POLITECNICO DI TORINO
Repository ISTITUZIONALE

Experimental assessment and validation of energy-maximising moment-based optimal control for a prototype wave energy converter

Original
Experimental assessment and validation of energy-maximising moment-based optimal control for a prototype wave energy converter / Faedo, N; Pena-Sanchez, Y; Garcia-Violini, D; Ferri, F; Mattiazzo, G; Ringwood, Jv. - In: CONTROL ENGINEERING PRACTICE. - ISSN 0967-0661. - 133:(2023), p. 105454. [10.1016/j.conengprac.2023.105454]

Availability:
This version is available at: 11583/2979755 since: 2023-06-30T14:32:15Z

Publisher:
PERGAMON-ELSEVIER SCIENCE LTD

Published
DOI:10.1016/j.conengprac.2023.105454

Terms of use:

This article is made available under terms and conditions as specified in the corresponding bibliographic description in the repository

Publisher copyright

(Article begins on next page)

29 April 2024

Control Engineering Practice 133 (2023) 105454

Contents lists available at ScienceDirect

Control Engineering Practice

journal homepage: www.elsevier.com/locate/conengprac

Experimental assessment and validation of energy-maximising moment-based optimal control for a prototype wave energy converter

Nicolás Faedo [a,*], Yerai Peña-Sanchez [f], Demián Garcia-Violini [d,e], Francesco Ferri [c], Giuliana Mattiazzo [a], John V. Ringwood [b]

[a] Marine Offshore Renewable Energy Lab, Department of Mechanical and Aerospace Engineering, Politecnico di Torino, Turin, Italy
[b] Centre for Ocean Energy Research, Maynooth University, Maynooth, Ireland
[c] Department of the Built Environment, Aalborg University, Aalborg, Denmark
[d] Departamento de Ciencia y Tecnología, Universidad Nacional de Quilmes, Buenos Aires, Argentina
[e] Consejo Nacional de Investigaciones Científicas y Técnicas (CONICET), Buenos Aires, Argentina
[f] Department of Mathematics, Euskal Herriko Unibertsitatea (EHU/UPV), Leioa, Spain

ARTICLE INFO

Keywords:
Wave energy
Experimental validation
Energy-maximising control
Optimal control
Moment
Moment-matching

ABSTRACT

In recent years, a framework for control of wave energy converters (WECs), termed *moment*-based control, has been developed within the wave energy conversion literature, exhibiting a remarkable performance in terms of energy absorption, while retaining real-time computational capabilities. Nonetheless, to date, practical results regarding moment-based control for WEC systems have been exclusively provided in numerical simulation, *i.e.* there is currently a lack of 'real-world' assessment of this promising control framework. Motivated by this, we present, in this paper, an experimental assessment and validation of moment-based WEC control for a prototype Wavestar wave energy converter, at the tank-testing facilities of Aalborg University, Denmark. In particular, we address the control design and synthesis procedure in an integrated fashion, covering experimental (physically consistent) system identification, unknown-input estimation and forecasting of wave excitation force, and subsequent control law implementation. We demonstrate that the moment-based controller is able to effectively maximise energy absorption from the wave resource in real-time, with a significant and consistent improvement with respect to the defined benchmark case. The results presented and discussed in this paper demonstrate the feasibility of moment-based WEC control, filling the gap between the attractive theoretical aspects associated with such a strategy, and the practical WEC energy conversion application.

1. Introduction

Commercial success of wave energy converters (WECs) intrinsically depends upon the availability of tailored control system technology, capable of maximising the wave energy extraction capabilities of a general class of devices, in a potentially wide variety of resource (*i.e.* sea-state) conditions (Ringwood, 2020; Ringwood, Bacelli, & Fusco, 2014). To be precise, any suitable controller for a WEC system must maximise energy conversion from incoming waves with real-time capabilities, while guaranteeing, at the same time, consistent satisfaction of any physical limitations underlying the mechanical device itself, and the power take-off (PTO) actuator system. The formulation of the control problem for WEC systems can be naturally regarded as being 'non-traditional', since the design objective departs significantly from classical tracking/regulation objectives.

In fact, not only does the energy-maximising control problem for WECs fall outside standard control formulations, but it is also, at its core, an inherently non-causal problem (see *e.g.* Faedo, Carapellese, Pasta, & Mattiazzo, 2022; Scruggs, Lattanzio, Taflanidis, & Cassidy, 2013), requiring both instantaneous and future information of the force/torque exerted by the (panchromatic) wave resource for the computation of the corresponding optimal law, further complicating the real-time WEC control landscape. This essentially translates to an intrinsic requirement of unknown-input estimation techniques (Peña-Sanchez, Windt, Davidson, & Ringwood, 2019), to provide instantaneous estimates of the wave excitation, and forecasting strategies (Peña-Sanchez, Mérigaud, & Ringwood, 2018), able to predict future values within a certain time interval, which are fed to the controller so as to effectively achieve energy-maximising optimality conditions.

An increasing number of candidate solutions for such a control problem have been proposed within the wave energy conversion literature, with (economic) model predictive control (MPC) being the first solid

* Corresponding author.
E-mail address: nicolas.faedo@polito.it (N. Faedo).

https://doi.org/10.1016/j.conengprac.2023.105454
Received 13 June 2022; Received in revised form 10 October 2022; Accepted 31 January 2023
Available online 9 February 2023
0967-0661/© 2023 The Authors. Published by Elsevier Ltd. This is an open access article under the CC BY license (http://creativecommons.org/licenses/by/4.0/).

aspirant (making an early formal appearance in 2010 by Cretel, Lewis, Lightbody, and Thomas (2010)). Nonetheless, 'pure' energy-maximising MPC formulations tend to be inherently non-convex (Faedo, 2020; Faedo, Olaya, & Ringwood, 2017), often requiring modifications of the underlying control objective function to guarantee well-posedness, *i.e.* existence of globally optimal solutions. Furthermore, real-time implementation of energy-maximising MPC for WEC systems has been found to be challenging (see *e.g.* Li & Belmont, 2014; Richter, Magana, Sawodny, & Brekken, 2012), though some degree of improvement has been reported in recent numerical (re)formulations, *e.g.* Tona, Sabiron, Nguyen, Mérigaud, and Ngo (2020) and Zhan, Li, and Bailey (2019). Given the intrinsic degree of complexity underpinning WEC control problems, experimental assessment and validation of MPC, and, in fact, any class of energy-maximising WEC controllers, comprising unknown-input estimation, forecasting, and effective real-time controller calculations, is rather scarce. This is, nevertheless, a fundamental stepping stone to demonstrate the concrete feasibility of any candidate WEC controller in realistic scenarios. Among the few exceptions that effectively provide a complete experimental assessment of optimal (particularly MPC-based) WEC control, including wave excitation estimation/forecast, within wave tank facilities, the reader is referred to[1] Nguyen, Sabiron, Tona, Kramer, and Vidal Sanchez (2016), Tona et al. (2020) and Umeda, Goto, Fujiwara, Taniguchi, and Inoue (2018).

The apparent limitations of MPC for the wave energy conversion problem led researchers to explore the more general pool of direct optimal control techniques, leveraging a variety of global/semi-global discretisations of state and input variables, leading to more efficient computational formulations. Examples include spectral (Galerkin) methods, *e.g.* Bacelli and Ringwood (2014) (finite-dimensional Fourier series), pseudospectral (collocation) techniques, *e.g.* Li (2017) (Legendre polynomials) and Genest and Ringwood (2016) (half-range Chebyshev–Fourier polynomials), and the system-theoretic approach termed *moment-based* control, which is the central topic of this paper.

Moment-based control for WEC systems, presented for the first time in Faedo, Scarciotti, Astolfi, and Ringwood (2018), is based upon the system-theoretic notion of a *moment*, originally defined within the field of model order reduction in Astolfi (2010) (see also Astolfi, Scarciotti, Simard, Faedo, & Ringwood, 2020). In particular, moments are mathematical objects which share a strong connection with the steady-state behaviour of the wave energy conversion system. As such, they offer an efficient parameterisation of the related state and input variables, leading to a well-posed transcription of the target (infinite-dimensional, see Section 4.1) optimal control problem, with guarantees of existence and uniqueness of globally optimal solutions. Research on moment-based WEC control has evolved significantly since the first theoretical grounds presented in Faedo et al. (2018), with advances in *e.g.* nonlinear (Faedo, Giorgi, Ringwood, & Mattiazzo, 2022; Faedo, Scarciotti, Astolfi, & Ringwood, 2021b) (consistent approximation of moments for nonlinear systems and extension of moment-based theory to a general class of nonlinear WEC systems, respectively), robust (Faedo, García-Violini, Scarciotti, Astolfi, & Ringwood, 2019; Faedo, Mattiazzo, & Ringwood, 2022) (moment-based control under system and input uncertainty, respectively), and receding-horizon (Faedo, Peña-Sanchez, & Ringwood, 2020) formulations, demonstrating that the moment-based theory effectively fits well with the WEC control application, and can be exploited to efficiently solve the associated optimal control problem.[2]

Nonetheless, to date, practical results regarding moment-based control for WEC systems are exclusively provided in numerical simulation environments,[3] *i.e.* there is a lack of experimental assessment and validation of such a control framework. This is, as argued previously in this section, fundamental to demonstrating the concrete feasibility of any WEC control technique in realistic scenarios, hence providing tangible proof of reliability of moment-based control for any candidate WEC technology stakeholder.

In the light of the potential demonstrated by moment-based control in achieving optimal energy-maximising conditions for WEC systems, and the intrinsic requirement of 'real-world' testing for its reliable utilisation, we provide, in this paper, a comprehensive experimental assessment and validation of such an energy-maximising control strategy for WEC devices. To achieve this objective, we consider a prototype of the Wavestar WEC system (Hansen & Kramer, 2011), available within the tank-testing facilities of the Department of the Built Environment, Aalborg University, Denmark. The choice of this particular experimental prototype and setup is motivated by the fact that this same system and configuration has been previously adopted as an experimental benchmark case for WEC control testing, specifically within the first edition of the so-called Wave Energy Control Competition (WEC^{3}OMP), as described in Ringwood, Ferri, Ruehl, Yu, Coe, Bacelli, Weber, and Kramer (2017) and Ringwood, Ferri, et al. (2019), demonstrating its suitability and representativeness for testing energy-maximising control algorithms.

To be precise, this paper presents, to the best of our knowledge, the *first* experimental assessment and validation of moment-based control for WEC systems, incorporating design, synthesis, and real-time implementation procedures, hence filling the gap between the theoretical aspects associated with such a control framework, and the corresponding practical application. Our contributions include experimental system identification of the WEC system (leading to a suitable model for control and estimation purposes) and its corresponding model validation; design, synthesis, and validation of the unknown-input estimator and forecasting strategies adopted, required to provide instantaneous and future estimates of the wave resource for control calculations, respectively; and tuning, implementation, and validation of the integrated moment-based control architecture. Via a detailed performance assessment, we demonstrate that moment-based WEC control has excellent capabilities for maximising energy absorption in realistic conditions, significantly outpeforming a widely adopted benchmark controller case, hence directly validating the potential of this technique in the pathway towards commercialisation of WEC systems.

The reminder of this paper is organised as follows. Section 1.1 introduces the notation adopted throughout our study. Section 2 presents the prototype WEC system, and the corresponding experimental setup, including a description of the facilities available at the testing site. Section 3 describes the system identification procedure adopted to compute a control-oriented model of the WEC system, based upon experimental data. Section 4 provides an integrated account of the control design and synthesis procedure, including a formal definition of the optimal control problem for WECs, a summary of direct transcription via moment-based theory, and presentation of the unknown-input estimation and forecasting techniques used to provide instantaneous and future estimates of the force exerted by the wave resource. Section 5 offers a thorough description, analysis, and performance assessment of the integrated control architecture, including a comparison (in terms of energy absorption) with a benchmark controller, while Section 6 encompasses the main conclusions of our study. Finally, we note that open-access multimedia material, related to the experimental campaign and results presented within this manuscript, has been made accessible by the authors in *WavEnergy Wiki* (2022) and *WavEnergy YouTube Channel* (2022).

[1] Other MPC-based solutions, tested experimentally, can be found in *e.g.* Ling, Bosma, and Brekken (2019) and Tom and Yeung (2015), though these studies simplify the design procedure by either disregarding the wave excitation within the control design procedure (hence being inherently sub-optimal), or by assuming that measurements of wave elevation/excitation are effectively available, which is effectively not feasible in practice (Peña-Sanchez et al., 2019).

[2] The reader is referred to Faedo and Ringwood (2021) for a comprehensive overview of moment-based methods for wave energy conversion applications.

[3] Although also including high-fidelity testing in computational fluid dynamics (CFD) solvers, see Windt, Faedo, Penalba, Dias, and Ringwood (2021).

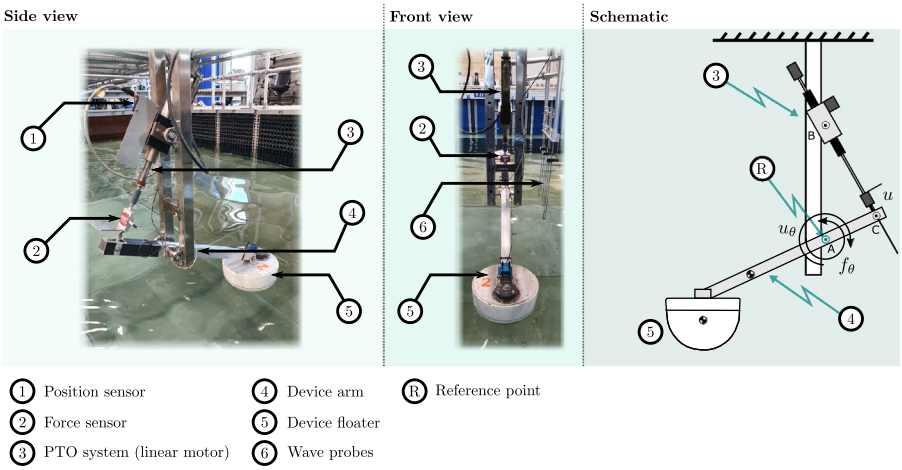

Fig. 1. Experimental WEC system considered.

1.1. Notation

$\mathbb{R}^+$ is used for the set of non-negative real numbers, while $\mathbb{C}_{<0}$ and $\mathbb{C}^0$ denote the sets of complex numbers with strictly negative, and zero real part, respectively. Unless stated otherwise, the symbol 0 stands for any zero element, dimensioned according to the context. $\mathbb{N}_Q$ denotes the set of positive numbers up to $Q \in \mathbb{N}$, *i.e.* $\mathbb{N}_Q = \{1, 2, \dots, Q\}$. The symbols $\mathbb{I}_n$ and $\mathbf{1}_{n\times m}$ are used to denote the standard identity matrix of the space $\mathbb{C}^{n\times n}$, and the Hadamard identity matrix in $\mathbb{C}^{n\times m}$, respectively. The spectrum of a matrix $A \in \mathbb{C}^{n\times n}$ is denoted as $\lambda(A) \subset \mathbb{C}$, while A^T is used to denote the transpose of A The symbol $\bigoplus$ indicates the direct sum of matrices, *i.e.* $\bigoplus_{i=1}^{n} A_i = \text{diag}(A_1, \dots, A_n)$. The Kronecker product is denoted with its usual symbol $\otimes$. The Laplace transform of a function f (provided it exists) is denoted as $F(s)$, $s \in \mathbb{C}$, while its Fourier transform is denoted consistently with the restriction of the domain of F to $\mathbb{C}^0$, *i.e.* $F(j\omega)$, with $\omega \in \mathbb{R}$.

2. Experimental WEC system and setup

We briefly describe, in this section, the experimental WEC system considered within this study, located within the tank-testing facilities available at Aalborg University, Denmark.[4] The device, shown in Fig. 1, corresponds to a 1:20th scale prototype of a single floater of the so-called Wavestar WEC system (see *e.g.* Hansen & Kramer, 2011), and has been custom made and designed by Aalborg University. The WEC is free to move in a single degree-of-freedom (DoF), with the floater arm standing at ≈ 30 [°] with respect to the horizontal reference frame in its equilibrium position. The PTO (actuator) system is an electrical, direct drive, motor (*LinMot Series P01-37 x 240F*), sitting on the upper structural joint composing the device (see Fig. 1). The corresponding drive is a *LinMot E1200*, with a force rating up to ±200 [N]. The main parameters, characterising the WEC system, can be found in Table 1.

Translational displacement (associated with the PTO system) is measured via a dedicated laser position sensor (*MicroEpsilon ILD-1402-600*), while the total force exerted on the PTO axis is measured by means of a *S-beam Futek LSB302* load cell. The system is equipped with a dual-axis accelerometer (*Analog Devices ADXL203EB*), which is explicitly used to derive measures of rotational motion (*i.e.* angular displacement and velocity) about the fixed reference point A (see schematic in Fig. 1). Data acquisition is implemented using a rapid prototyping hardware architecture (see Fig. 2), with the controller being implemented in real-time using MATLAB SIMULINK®. The specific

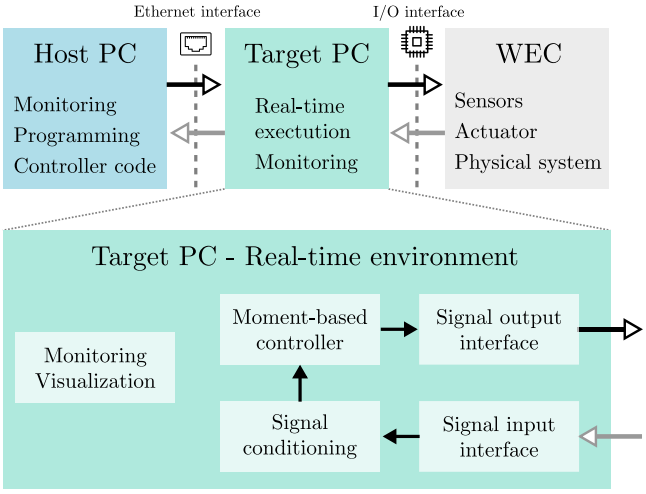

Fig. 2. Schematic illustration of used software and hardware architecture.

Table 1
WEC parameters.

Parameter	Value (including units)
Floater mass	4 [kg]
Floater moment of inertia	1 [kg m^2]
Floater draft	0.110 [m]
Floater diameter at SWL	0.256 [m]
Distance points A-B	0.412 [m]
Distance points B-C	0.381 [m]
Distance points A-C	0.200 [m]
Arm mass	1.157 [kg]
Arm moment of inertia	0.060 [kg m^2]

input/output (I/O) acquisition board is a *National Instruments NI PCI-6221 DAQ*. The WEC system is connected to the *target PC* (running on a real-time operating system) via the corresponding I/O board, with a sampling rate of 1 [kHz], while the communication between target and *host PC* (which effective compiles the moment-based controller code) is achieved via a standard Ethernet connection.

The physical wave-tank facility is schematically illustrated in Fig. 3. The wave basin features a total length of 14.5 [m], with a corresponding width of approximately 13 [m]. The wavemaker, used to generate the sea-states considered to evaluate the performance of the controller (see Section 5.1), is composed of 30 (individually controlled) wave paddles (manufactured by *VTI systems*), used within this study to produce long-crested waves with the paddles acting in unison. The

[4] The interested reader is referred to Pena-Sanchez, García-Violini, and Faedo (2022) for an interactive video featuring an overview of the wave tank testing facilities and prototype WEC system by the authors.

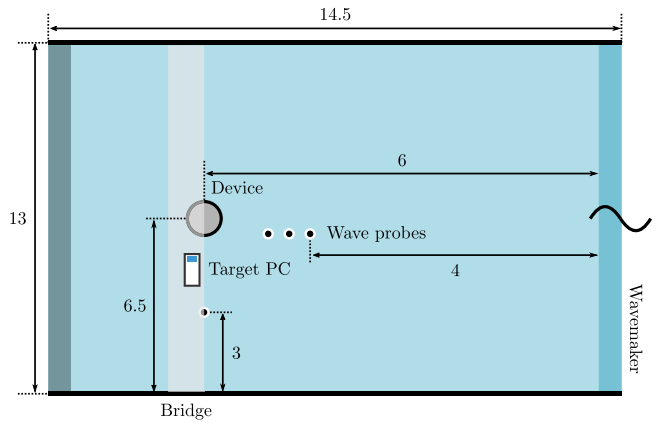

Fig. 3. Schematic illustration of the wave-tank facility at Aalborg University. Dimensions are in metres.

device is sitting at (approximately) the mid-point (in width) of the basin, mounted on a bridge spanning the full width of the tank, as in Fig. 3. Finally, consistency of the generated free-surface elevation, and evaluation of any potential radiated waves, are measured by means of different sets of resistive wave probes (*VTI WG-8CH* - see Fig. 1), located as depicted in Fig. 3.

3. Experimental WEC modelling

Following standard potential flow theory assumptions[5] (see *e.g.* Falnes & Kurniawan, 2020; Korde & Ringwood, 2016), we consider that the WEC system, described in Section 2, can be modelled in terms of a linear operator $G_\theta : \mathbb{C} \to \mathbb{C}$, $s \mapsto G_\theta(s)$, describing the *rotational dynamics* of the wave conversion system about the fixed reference point A (see schematic in Fig. 1), *i.e.*

$$V_\theta(s) = G_\theta(s)\left(F_\theta(s) - U_\theta(s)\right), \tag{1}$$

where $v_\theta(t) \in \mathbb{R}$, denotes the angular (pitch) velocity of the WEC floater arm, $f_\theta(t) \in \mathbb{R}$ is the wave excitation torque (external uncontrollable input due to the action of the incoming wave field on the device floater), and $u_\theta(t) \in \mathbb{R}$ denotes the torque exerted by the PTO (control) system at the reference point A, to be optimally designed to achieve maximum energy absorption from the wave resource.

Remark 1. As discussed in *e.g.* Ringwood, Mérigaud, Faedo, and Fusco (2019), the performance of energy-maximising WEC controllers is directly affected by the accuracy of the mathematical representation G_θ, used for control design purposes. Common practice within the wave energy modelling/control field is to compute a parametric expression for G_θ in (1) based on *physical* principles, in particular by leveraging numerical boundary-element-method (BEM) hydrodynamic solvers (see *e.g.* the well-known open-source software Nemoh (Babarit & Delhommeau, 2015)). Nonetheless, (physical) BEM methods provide a linear characterisation of the WEC (hydro)dynamics under the assumption of infinitesimally small motion of the system about the zero-equilibrium position (see Davidson, Giorgi, & Ringwood, 2015; Faedo, Piuma, Giorgi, & Ringwood, 2020). Given that the control design objective for WECs is that of *maximising converted energy* (see Section 4.1), which typically implies an enhancement of device motion, BEM-based methods are likely to produce non-representative linear models of the WEC dynamics, almost inevitably leading to degraded control performance (see Windt et al., 2021). Furthermore, the experimental WEC system is, naturally, 'non-ideal', *i.e.* it presents physical effects/dynamical behaviour unmodelled by BEM-based methods, which focus solely on the hydrodynamics associated with the mechanical energy conversion process. This includes any significant PTO motor dynamics, mechanical friction effects in the joints, and structural vibration, among others.

An alternative path, to that discussed in Remark 1, is that provided within the field of system identification,[6] which can be generally divided into two main subcategories: *Grey-box*, and *black-box* system identification. Grey-box-identification techniques employ a model structure (assumed known), typically inspired by physical considerations, for which a set of system parameters are tuned using observed (experimental/numerical) data. In contrast, when the model structure is not known, and the identification is based entirely on observed data, the approach is known as black-box-identification. Generally, as discussed in *e.g.* Beatty, Hall, Buckham, Wild, and Bocking (2015), Davidson et al. (2015) and García-Violini, Pena-Sanchez, Faedo, Windt, and Ringwood (2020), a black-box methodology allows for a more accurate model description and, consequently, more efficient controller designs. Furthermore, being directly based upon experimental data from the WEC process, the black-box identification approach allows for the intrinsic inclusion of dynamics completely neglected when following the BEM approach, such as any significant PTO motor dynamics, mechanical friction effects in the joints, and structural vibration (see the discussion provided in Remark 1).

Motivated by the arguments exposed in this section, we pursue a black-box system identification approach to compute a *representative* linear model G_θ, able to characterise the experimental WEC dynamics in a control-oriented form, for the set of defined operating (sea-state) conditions. Before presenting the corresponding system identification procedure, we note that the map G_θ should exhibit a number of structural (dynamical) properties, related to the physics of the WEC process. These properties, which are fundamental to guarantee well-posedness of the moment-based direct optimal control transcription (see Section 4.2), are as follows:

(P1) G_θ is bounded-input bounded-output (BIBO) stable.
(P2) G_θ is strictly proper.
(P3) G_θ is positive-real.

As already stated in the previous paragraph, properties (P1), (P2), and (P3) above follow from physical grounds (see *e.g.* Faedo, Carapellese, et al., 2022; Scruggs et al., 2013). Briefly summarising: (P1) can be effectively derived straightforwardly, since the zero-equilibrium of the WEC system is locally exponentially stable; (P2) follows from the fact that the WEC device has a non-zero inertia; while (P3) is equivalent to asserting that the (stable) WEC system does not encompass any non-conservative internal energy source/s that can influence its I/O behaviour. Note that (P3) is, in fact, related to the intrinsic *passivity* property implied by the physics of the WEC system, and is fundamental to guarantee well-posedness[7] of the control design procedure (see Remark 7).

3.1. WEC system identification

As introduced in Section 3, we adopt a black-box system identification procedure to compute a representative WEC model G_θ, based on a tailored design of I/O experiments and the subsequent application of frequency-domain identification techniques. Such a procedure is described in the following.

[5] The same assumptions have been adopted within the WEC^{3}OMP (Ringwood et al., 2017).

[6] The reader is referred to *e.g.* Ljung (1998) for a thorough introduction to the field of system identification.

[7] The relation between passivity and well-posedness of WEC control design is not unique to the strategy proposed in this paper, but effectively extends among diverse WEC control design procedures (see *e.g.* Bacelli & Ringwood, 2014; Jia, Meng, Dong, Liu, Sun, & Dong, 2020; Scruggs et al., 2013).

Let $f_{\mathrm{id}}(t) \in \mathbb{R}$ be a normalised *down-chirp* signal, designed to excite the WEC system within a frequency band $\Omega \subset \mathbb{R}^+$, with a total time-length denoted by $T_{\mathrm{id}} \in \mathbb{R}^+$. Let $\mathcal{A} = \{A_i\}_{i=1}^{Q} \subset \mathbb{R}^+$ be an associated set of $Q \in \mathbb{N}/0$ input amplitudes, and let $\mathcal{U} = \{A_i f_{\mathrm{id}}(t)\}_{i=1}^{Q} \subset \mathbb{R}$ be the corresponding set of input signals. Without the presence of waves in the tank, *i.e.* in still waters, we proceed to inject each exciting input signal, belonging to the set $\mathcal{U}$, as a force command via the PTO (motor) system, producing a corresponding set of angular velocity outputs $\mathcal{Y}_\theta = \{y_{\theta_i}(t)\}_{i=1}^{Q}$.

Remark 2. Given that we are interested in the rotational dynamics of the device (see Eq. (1)), it is straightforward to note that, by means of a simple algebraic map[8] $\tau : \mathbb{R} \to \mathbb{R}$, $A_i f_{\mathrm{id}}(t) \mapsto \tau(A_i f_{\mathrm{id}}(t)) = f_{\mathrm{id}_{\theta_i}}(t)$, we can "convert" the set of input forces $\mathcal{U}$ to torque signals acting on the floater arm, producing a corresponding set of input torques $\mathcal{U}_\theta = \{f_{\mathrm{id}_{\theta_i}}(t)\}_{i=1}^{Q}$.

Remark 3. The choice of down-chirp experiments, as opposed to the 'more classical' up-chirp case (considered in *e.g.* García-Violini, Peña-Sanchez, Faedo, Windt, Ferri, & Ringwood, 2021), is merely adopted to minimise the effect of reflected waves within the wave basin during the identification procedure.

Having computed the sets $\mathcal{U}_\theta$ and $\mathcal{Y}_\theta$, we define the so-called empirical transfer function estimates (ETFEs) $G_{\mathrm{id}_i} : \mathbb{C}^0 \to \mathbb{C}$, $\jmath\omega \mapsto G_{\mathrm{id}_i}(\jmath\omega)$, for each I/O pair $(f_{\mathrm{id}_{\theta_i}}(t), y_{\theta_i}(t)) \in \mathcal{U}_\theta \times \mathcal{Y}_\theta$, *i.e.*

$$G_{\mathrm{id}_i}(\jmath\omega) = Y_{\theta_i}(\jmath\omega) \Big/ F_{\mathrm{id}_{\theta_i}}(\jmath\omega), \tag{2}$$

with $i \in \mathbb{N}_Q$. With the definition provided in Eq. (2), we can readily compute the so-called *average* ETFE $\bar{G}_{\mathrm{id}}(\jmath\omega)$, with the aim of building a low-variance representative set to use as input to the chosen frequency-domain identification procedure (see Ljung, 1998). In particular, the expression for $\bar{G}_{\mathrm{id}}$ is

$$\bar{G}_{\mathrm{id}}(\jmath\omega) = \frac{1}{Q}\sum_{i=1}^{Q} G_{\mathrm{id}_i}(\jmath\omega). \tag{3}$$

The average ETFE in (3) is then used to compute a continuous-time, minimal, internally stable, strictly proper, state-space system $G_{\mathrm{id}} \equiv (A_{\mathrm{id}}, B_{\mathrm{id}}, C_{\mathrm{id}})$, with $A_{\mathrm{id}} \in \mathbb{R}^{n\times n}$, $\{B_{\mathrm{id}}, C_{\mathrm{id}}^{\mathsf{T}}\} \subset \mathbb{R}^n$, via standard subspace-based system identification procedures (see Van Overschee & De Moor, 2012). Regarding the specific design parameters used to compute (3), the frequency band for the design of f_{id} is set to $\Omega = [0.01, 50]$ [rad/s] (which fully covers the typical operational range of the WEC system), with a time-length of $T_{\mathrm{id}} = 140$ [s]. The set of input amplitudes is set to $\mathcal{A} = \{2.5, 5, 7.5, 10, 12.5\}$ [N] (and hence $Q = 5$), while the order (dimension) associated with the identified state-space structure G_{id} is set to $n = 8$.

The results of the system identification procedure,[9] described above, are summarised in Fig. 4. In particular, Fig. 4 shows the ETFE associated with each corresponding experimental I/O pair (dotted-grey lines), together with the frequency-response map corresponding with the identified system G_{id} (dot-dashed-black line), and the characterisation of G_θ in (1) computed via BEM-based[10] hydrodynamic codes (dashed-red line). As expected from the arguments exposed in Remark 1, it can be appreciated that the BEM-based model effectively misrepresents the dynamical behaviour of the WEC system, featuring a shifted resonance frequency, and hence presenting considerable difference in magnitude and phase within the operating (wave) frequency range.

[8] The map τ depends on the geometry of the arm, and each specific length involved (see Ringwood et al., 2017). We omit its explicit derivation for the sake of brevity.

[9] Multimedia content regarding the system identification procedure, performed to compute G_θ within this study, can be found in García-Violini, Faedo, and Pena-Sanchez (2022).

[10] The open-source software Nemoh (Babarit & Delhommeau, 2015) has been used to compute the BEM-based model.

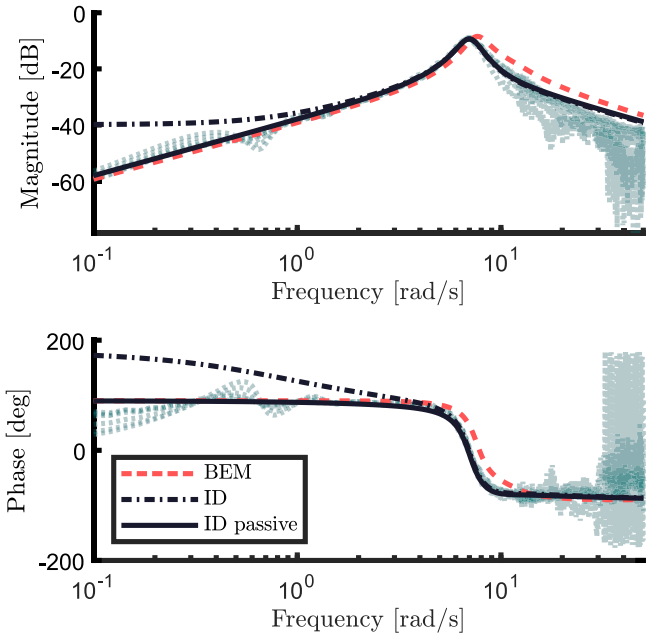

Fig. 4. Bode plot associated with each experimental ETFE (dotted-grey), BEM-based model (dashed-red), identified system G_{id} (dot-dashed-black), and passivised system G_θ (solid-black).

3.2. Model passivation

The model identified in Section 3.1, G_{id}, respects two of the structural (physical) properties associated with (1), discussed in Section 3. In particular, while G_{id} is both BIBO stable (P1) and strictly proper (P2), its associated transfer function is not positive-real (P3), *i.e.* the identified system *is not passive*. Given the relevance of this model property in the design of the energy-maximising optimal controller (see Section 4.2 and Remark 7), we proceed to *passivise* G_{id} based upon the introduction of a suitably designed model *output* perturbation ΔC_{id}, following Faedo, Peña-Sanchez, Carapellese, Mattiazzo, and Ringwood (2021). In particular, we define the passivised system G_θ as

$$G_\theta : \begin{cases} \dot{x} = Ax + B(f_\theta - u_\theta), \\ v_\theta = Cx, \end{cases} \tag{4}$$

with $A = A_{\mathrm{id}}$, $B = B_{\mathrm{id}}$, $C = C_{\mathrm{id}} + \Delta C_{\mathrm{id}}$, and where the perturbation $\Delta C_{\mathrm{id}}^{\mathsf{T}} \in \mathbb{R}^n$ is designed to enforce system G_θ to be passive, while minimising, at the same time, its impact on the overall dynamics of the identified map G_{id}, *i.e.* while minimising $\|\Delta C_{\mathrm{id}}\|_2$. The specific computation of ΔC_{id} is achieved by solving Faedo, Peña-Sanchez, et al. (2021, Problem 2), with the software implementation in Faedo (2021), which enforces the well-known set of positive-realness linear matrix inequality (LMI) conditions arising from the Kalman–Yakubovich–Popov lemma.

The results of applying the passivation procedure in Faedo, Peña-Sanchez, et al. (2021) (briefly described above), can be appreciated in both Figs. 4 and 5. In particular, as can be seen in Fig. 4, the frequency response of G_θ (solid-black line) is almost indistinguishable from G_{id} in the neighbourhood characterising the dominant WEC dynamics (*i.e.* close to the resonance frequency), but 'corrects' the non-passive behaviour in the low frequency band. This can be appreciated with greater detail in Fig. 5, which illustrates the frequency response associated with the so-called *scattering representation* (see *e.g.* Desoer & Vidyasagar, 2009) of both the identified system G_{id} (dot-dashed-black line), and the corresponding passivised structure G_θ (solid-black line). It can be seen that the latter scattering representation has a $\mathscr{H}_\infty$-norm ≤ 1 (*i.e.* defined below the 0 [dB] line), which is a well-known condition for passivity in LTI systems (Desoer & Vidyasagar, 2009). In contrast, the former shows a passivity violation in the low frequency band, as expected from inspecting Fig. 4.

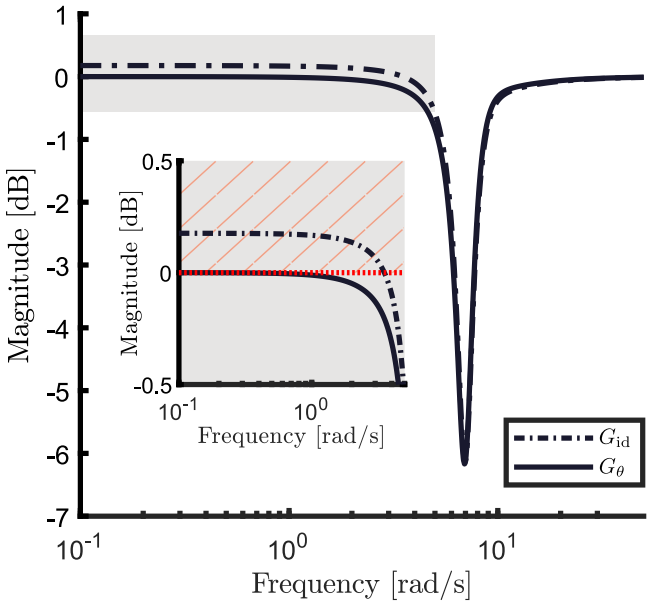

Fig. 5. Frequency response (in magnitude) associated with the scattering representation of the identified system G_{id} (dot-dashed-black), and the passivised WEC model G_θ (solid-black). The horizontal red line denotes the 0 [dB] line.

4. Energy-maximising moment-based control

Within this section, and based on the experimental WEC model G_θ in (4), we briefly present the fundamentals behind moment-based control for WEC systems, together with the adopted unknown-input estimation technique, and wave excitation forecasting algorithm. In particular, Section 4.1 provides a formal definition of the energy-maximising WEC control problem, while Section 4.2 offers a brief account of direct transcription via moment-based theory. Finally, Section 4.3 describes the computation of instantaneous and future wave excitation values, required by the WEC controller, and their corresponding incorporation and use within moment-based control calculations.

4.1. Definition of the WEC control problem

The control problem for WEC systems can be described in terms of an optimal control problem (OCP), which essentially aims to maximise energy absorption from the incoming wave resource. In particular, throughout this paper, we adopt a receding-horizon approach for the definition of the associated OCP, motivated both by wave excitation estimation and forecasting requirements, and the intrinsic necessity of real-time control operation (see *e.g.* Faedo et al., 2017; Genest & Ringwood, 2016). Let $T_h \in \mathbb{R}^+$ denote the so-called time-horizon, in which energy is effectively optimised within a corresponding receding time-window $\Xi_N = [N\Delta_h, N\Delta_h + T_h] \subset \mathbb{R}^+$, $N \in \mathbb{N}/0$, by means of an optimal control input $u_\theta^{\text{opt}} : \Xi_N \to \mathbb{R}$, and where Δ_h denotes the receding time-step (*i.e.* controller sampling time). Considering mechanical energy generation as the main control objective, we can define the following objective function

$$\mathscr{E}_N(u_\theta) \mapsto \frac{1}{T_h}\int_{\Xi_N} u_\theta(\tau)v_\theta(\tau)\mathrm{d}\tau, \tag{5}$$

where the integrand in (5) represents instantaneous mechanical power within the time-window Ξ_N. In addition, and taking into consideration the intrinsic physical limitations of the prototype system presented in Section 2, we define the following set of state and input constraints

$$\mathscr{C}_\theta : \{|z_\theta| \le Z_{\max}, \quad |u_\theta| \le U_{\max}, \tag{6}$$

$\forall t \in \Xi_N$, with $\{Z_{\max}, U_{\max}\} \subset \mathbb{R}^+$, and where $z_\theta = \int v_\theta$ denotes the rotational displacement of the WEC system. Note that, as explicitly discussed in Section 1, the experimental setup and system considered within this paper has been previously chosen as an experimental benchmark case for WEC control testing, specifically within the first edition of the WEC^{3}OMP (Ringwood et al., 2017; Ringwood, Ferri, et al., 2019). As such, the nature of both the physical WEC limitations, and PTO characteristics, described in the set of constraints (6), coincide with those adopted within the benchmark control case provided by the WEC^{3}OMP, including specific numerical values for $\{Z_{\max}, U_{\max}\}$ (see Section 5.4).

With the definitions provided in (5)–(6), the specific receding-horizon OCP (P_N), for the WEC system described in Section 3, essentially consists of finding an optimal control law u_θ^{opt} for each window Ξ_N such that

$$\begin{aligned}(P_N) : u_\theta^{\text{opt}} = \arg\max_{u_\theta} \mathscr{E}_N(u_\theta),\\ \text{subject to:}\\ \text{WEC dynamics } G_\theta \text{ in (4)},\\ \text{State and input constraints } \mathscr{C}_\theta \text{ in (6)}.\end{aligned} \tag{7}$$

A summary of the receding-horizon WEC control procedure can be synthesised in the following three steps:

(1) $u_\theta^{\text{opt}} \leftarrow$ Solve (P_N) for the time-window Ξ_N.
(2) Apply u_θ^{opt} in the time-interval $[N\Delta_h, (N+1)\Delta_h]$.
(3) Move $\Xi_N \mapsto \Xi_{N+1}$ accordingly, and go back to (1).

4.2. Direct transcription via moment-based theory

Moment-based control, as developed and presented in a series of studies *e.g.* Faedo, Peña-Sanchez, and Ringwood (2020), Faedo et al. (2018) and Faedo, Scarciotti, Astolfi, and Ringwood (2021a) (see also the discussion provided in Section 1), has been shown to provide a tailored and convenient parameterisation of both control and state variables associated with the WEC system (4), which can be subsequently used to transcribe the infinite-dimensional OCP (P_N) in (7) to a well-posed and computationally tractable finite-dimensional nonlinear program (NP). In particular, leveraging the connection between *moments* and steady-state behaviour, the resulting NP can be shown to be of a concave (respectively convex) nature, facilitating real-time control implementation via convex finite-dimensional solvers. Although we refer the reader to the cited literature for a comprehensive and thorough derivation of the fundamentals behind moment-based control for WEC systems, we provide, in the following, a concise account of the main features and characteristics associated with such control strategy, with the final aim of keeping this paper reasonably self-contained.

The first fundamental feature of moment-based WEC control stems from the system-theoretic approach to model reduction by moment-matching presented in *e.g.* Astolfi (2010) and Astolfi et al. (2020), and entails the definition of a suitable implicit form description for the set of (controllable and uncontrollable) inputs affecting the WEC system. In particular, we consider, for $t \in \Xi_N$, the following finite-dimensional *signal generator*,

$$\mathcal{G}_\theta : \begin{cases}\dot{\xi} = S\xi,\\ f_\theta = L_f\xi,\\ u_\theta = L_u\xi,\end{cases} \tag{8}$$

with initial condition $\xi(N\Delta_h) \equiv \xi_0 \in \mathbb{R}^\nu$, $\nu \in 2\mathbb{Z}/0$, where $\{\xi(t), L_f^\mathsf{T}, L_u^\mathsf{T}\} \subset \mathbb{R}^\nu$, and the matrix $S \in \mathbb{R}^{\nu\times\nu}$, defining the state-transition map in (8), is given by

$$S = \bigoplus_{p=1}^{d}\begin{bmatrix}0 & p\omega_0\\ -p\omega_0 & 0\end{bmatrix}, \tag{9}$$

with $\nu = 2d$, $\lambda(S) = \{\pm\jmath p\omega_0\}_{p=1}^d \subset \mathbb{C}^0$, and where $\omega_0 = 2\pi/T_h$ is the so-called *fundamental frequency* associated with both f_θ and u_θ.

Remark 4. From now on, and without any loss of generality, we assume the triple of matrices $(S, \xi_0, L_f - L_u)$ is minimal, *i.e.* $(S, L_f - L_u)$ is observable and (S, ξ_0) is excitable.[11]

Remark 5. Let $\xi_i(t)$, with $i \in \mathbb{N}_\nu$, denote the ith entry of $\xi(t)$ in (8). Note that, given the excitability of (S, ξ_0),

$$\text{span}\left(\{\xi_i(t)\}_{i=1}^{\nu}\right) = \text{span}\left(\{\cos(d\omega_0), \sin(d\omega_0)\}_{p=1}^{d}\right), \tag{10}$$

and hence the implicit form system in (8) essentially describes f_θ and u_θ in terms of a T_h-periodic map in Ξ_N, composed of a (complete) set of d super-harmonic functions of ω_0.

The second characteristic of moment-based control concerns the exploitation of the concept of manifold invariance (Isidori, 2013), and steady-state output response of the system arising from the interconnection (8)–(4), *i.e.* the composite system $\mathscr{G}_\theta \circ G_\theta$. In particular, given that $\lambda(A) \subset \mathbb{C}_{<0}$ and $\lambda(S) \subset \mathbb{C}^0$ (with simple eigenvalues), there exists a unique matrix L_υ, with $L_\upsilon^\mathsf{T} \in \mathbb{R}^\nu$, such that the steady-state output response $\upsilon_{\theta_{ss}}$ of $\mathscr{G}_\theta \circ G_\theta$ is $\upsilon_{\theta_{ss}}(t) = L_\upsilon \xi(t)$, *i.e.* the steady-state output response of (8)–(4) can be fully described in terms of the solution ξ of the signal generator (8) (see Astolfi, 2010; Astolfi et al., 2020 for further detail).

Remark 6. The matrix L_υ is called the *moment* of system G_θ at the signal generator $\mathscr{G}$.

The explicit computation of L_υ follows from a specific Sylvester equation, which defines a centre manifold (hyperplane) for the composite system $\mathscr{G}_\theta \circ G_\theta$. In particular, it can be shown (Faedo, 2020; Faedo et al., 2018) that

$$L_\upsilon = \left(L_f - L_u\right) \Psi_\upsilon, \tag{11}$$

with $\Psi_\upsilon \in \mathbb{R}^{\nu \times \nu}$ defined as

$$\begin{aligned} \Psi_\upsilon^\mathsf{T} &= \left(\mathbb{I}_\nu \otimes C\right) \Psi^{-1} \left(\mathbb{I}_\nu \otimes -B\right), \\ \Psi &= \left(S \otimes \mathbb{I}_n\right) + \left(\mathbb{I}_\nu \otimes A\right), \end{aligned} \tag{12}$$

where invertibility of Ψ in (12), and hence uniqueness of the moment L_υ, is guaranteed by the condition $\lambda(A) \cap \lambda(S) = \emptyset$.

Using the implicit input description in (8), and the associated moment (11), the OCP (P_N) can be approximated, for each time-window Ξ_N, in terms of the following (Faedo, 2020; Faedo et al., 2018) finite-dimensional nonlinear program

$$\begin{aligned} \overline{(P_N)}: \; L_u^{\text{opt}} = \arg \max_{L_u^\mathsf{T} \in \mathbb{R}^\nu} & -\frac{1}{2} L_u \Phi_\upsilon L_u^\mathsf{T} + \frac{1}{2} L_f \Phi_\upsilon L_u^\mathsf{T}, \\ \text{subject to:} & \\ L_u \begin{bmatrix} \mathcal{A}_z & \mathcal{A}_u \end{bmatrix} &\leq \begin{bmatrix} \mathcal{B}_z & \mathcal{B}_u \end{bmatrix}, \end{aligned} \tag{13}$$

where the optimal control input is $u_\theta \leftarrow u_\theta^{\text{opt}} = L_u^{\text{opt}} \xi$, and the pairs of matrices $(\mathcal{A}_z, \mathcal{B}_z)$ and $(\mathcal{A}_u, \mathcal{B}_u)$, providing a finite-dimensional and convex description of the state (displacement) and input (control) constraints in (6), are defined following a direct collocation approach. In particular, by defining a set of $N_{\mathscr{C}}$ uniformly distributed collocation points $\mathcal{T}_{\mathscr{C}} = \{t_i^{\mathscr{C}}\}_{i=1}^{N_{\mathscr{C}}} \subset \Xi_N$, the convex constraints in (13) are such (Faedo, 2020; Faedo et al., 2018) that

$$\begin{aligned} &\mathcal{A}_z = -\Psi S^{-1} Y, \quad \mathcal{B}_z = Z_{\max} \mathbf{1}_{1 \times 2N_{\mathscr{C}}} + L_f \mathcal{A}_z, \\ &\mathcal{A}_u = Y, \qquad\qquad \mathcal{B}_u = U_{\max} \mathbf{1}_{1 \times 2N_{\mathscr{C}}}, \\ &Y = \begin{bmatrix} \Lambda & -\Lambda \end{bmatrix}, \quad \Lambda = \begin{bmatrix} \xi(t_1^{\mathscr{C}}) & \dots & \xi(t_{N_{\mathscr{C}}}^{\mathscr{C}}) \end{bmatrix}. \end{aligned} \tag{14}$$

Remark 7. The NP $\overline{(P_N)}$, arising via moment-based transcription, is in fact of a quadratic nature, *i.e.* a quadratic program (QP). Moreover, $\overline{(P_N)}$ is strictly concave (for any finite $\nu = 2d$ in (8)), *i.e.* the Hessian matrix $\mathscr{H} = 1/2(\Phi + \Phi^\mathsf{T})$ is positive definite, if and only if system G_θ is *passive* (see Faedo, 2020; Faedo et al., 2018).

[11] The reader is referred to Padoan, Scarciotti, and Astolfi (2017) for a formal treatment of this concept.

Note that the requirement elucidated in Remark 7, for well-posed ness of the adopted moment-based control approach, *i.e.* existence and uniqueness of solutions for problem $\overline{(P_N)}$ in (13) for each window Ξ_N, is always guaranteed within our study, by means of the passivation procedure for G_θ, described in Section 3.2. This, naturally, highlights the importance of deriving a physically representative model of the WEC system for control purposes. The concave QP nature of (13) directly implies that the moment-based control solution, parameterised in terms of L_u, can be computed in polynomial time (Vavasis, 2001), leveraging *e.g.* interior-point methods (see also Section 5.4).

Remark 8. The OCP formulated in (7), and transcribed into the finite-dimensional problem $\overline{(P_N)}$ via moment-based theory in (13), corresponds to the 'classical' (nominal) definition of the energy-maximising control problem for WEC systems, widely adopted in virtually all WEC-related control literature (see *e.g.* the review paper (Ringwood et al., 2014)). We note that a robust counterpart can be formulated using moments, by leveraging tools from robust optimisation theory, adopting a 'worst-case scenario' approach, in combination with a suitable definition of uncertainty. Though beyond the scope of this study, which has as a primary objective to provide, to the best of our knowledge, the first experimental assessment and validation of moment-based control for the classical energy-maximising WEC control objective (7) (see also the discussion provided in Section 1), we refer the interested reader to Faedo et al. (2019) and Faedo, Mattiazzo, and Ringwood (2022), for further details on robust moment-based control theory under system and input uncertainty, respectively.

4.3. Estimation and forecasting of wave excitation

Any attempt to solve the moment-based QP $\overline{(P_N)}$, defined in (13), requires full knowledge, *i.e.* *instantaneous* and *future* values, of the external uncontrollable input f_θ to resolve the WEC (dynamic) equality constraint, within the specified time-window Ξ_N, incorporated via a suitable definition of L_f in (8). Given the unmeasurable nature of the wave excitation (Peña-Sanchez et al., 2019), instantaneous values can be estimated via unknown-input observation techniques, while computation of future values requires prediction (*i.e.* forecasting) strategies, to 'extrapolate' the behaviour of the sea-state within Ξ_N. We discuss, in the following, the specific choice of such algorithms.

Guided by the performance results for wave excitation observers presented in Peña-Sanchez et al. (2019), unknown-input estimation is achieved, within this study, via a (steady-state) Kalman-Bucy filter (Kalman & Bucy, 1961), where the following 'extended' dynamical system

$$G_\theta^f : \begin{cases} \dot{x}_f = A_f x_f + B_f u_\theta + \varepsilon_{x_f}, \\ \upsilon_\theta = C_f x_f + \varepsilon_{\upsilon_\theta}, \end{cases} \tag{15}$$

is defined, where $x_f(t) = [x(t)^\mathsf{T} \; f_\theta(t)]^\mathsf{T} \in \mathbb{R}^{\tilde{n}}$, with $\tilde{n} = n + 1$, and $\varepsilon_{x_f}(t) \in \mathbb{R}^{\tilde{n}}$ and $\varepsilon_{\upsilon_\theta}(t) \in \mathbb{R}$ represent (white, zero-mean, mutually uncorrelated) process and measurement noise, respectively, with associated covariance matrices $Q_f \in \mathbb{R}^{\tilde{n} \times \tilde{n}}$ and $R_f \in \mathbb{R}$. The triple $(A_f, B_f, C_f^\mathsf{T}) \in \mathbb{R}^{\tilde{n} \times \tilde{n}} \times \mathbb{R}^{\tilde{n}} \times \mathbb{R}^{\tilde{n}}$ in (15) is given by

$$A_f = \begin{bmatrix} A & B \\ 0 & 0 \end{bmatrix}, \quad B_f = \begin{bmatrix} -B \\ 0 \end{bmatrix}, \quad C_f = \begin{bmatrix} C & 0 \end{bmatrix}. \tag{16}$$

Remark 9. The augmented system (15)–(16) is derived based on a *random walk* process for the (internal model) description of the wave excitation torque f_θ. The reader is referred to Nguyen and Tona (2017) for further details on this specific f_θ model selection.

The observer is hence given in terms of the following classical Luenberger structure

$$\widetilde{G_\theta^f} : \begin{cases} \dot{\widetilde{x_f}} = \left(A_f - L_f C_f\right) \widetilde{x_f} + L_f \upsilon_\theta + B_f u_\theta, \\ \widetilde{f_\theta} = C_{f_\theta} \widetilde{x_f}, \end{cases} \tag{17}$$

with $C_{f_\theta} = [0_{\tilde{n}}\ 1]$, $\widetilde{f_\theta}$ denotes the instantaneous estimate of f_θ, and where the observer gain in (17) can be computed as $L_f = P_f C_f^{\mathsf{T}} R_f^{-1}$, with $P_f = P_f^{\mathsf{T}} \in \mathbb{R}^{\tilde{n}\times\tilde{n}}$ the unique solution of the continuous-time algebraic Riccati equation

$$A_f P_f + P_f A_f^{\mathsf{T}} - P_f C_f^{\mathsf{T}} R_f^{-1} C_f P_f + Q_f = 0. \tag{18}$$

With respect to the computation of future, *i.e.* predicted, values of the wave excitation torque f_θ, we consider a variation of the classical auto-regressive (AR) model. In particular, we employ a direct multi-step (DMS) algorithm (Peña-Sanchez et al., 2018), avoiding the necessity of typical recurring AR iterations. To be precise, the p-step ahead predicted value of f_θ, denoted as $\widehat{f_\theta}[k+p|k] \in \mathbb{R}$, is computed as follows:

$$\widehat{f}[k+p|k] = \sum_{i=1}^{N_{\text{AR}}} \phi_i^p \widetilde{f_\theta}[k+1-i], \tag{19}$$

where $\widetilde{f_\theta}[k] \in \mathbb{R}$ denotes the excitation estimate $\widetilde{f_\theta}$, as computed in (17), at the kth sample, $N_{\text{AR}} \in \mathbb{N}/0$ is the order of the AR model, and the set $\Phi^p = \{\phi_i^p\}_{i=1}^{N_{\text{AR}}} \subset \mathbb{R}$ contains the regression coefficients corresponding with the p-step-ahead prediction. Given a set of 'training' data containing a sufficiently large $n_{\text{tr}} \in \mathbb{N}$ samples, the sets Φ^p are computed by minimising a separate objective function for each corresponding p, *i.e.*

$$\min_{\{\phi_i^p\}\subset\mathbb{R}} \sum_{k=N_{\text{AR}}+1}^{n_{\text{tr}}} \left(\widetilde{f_\theta}[k+p] - \sum_{i=1}^{N_{\text{AR}}} \phi_i^p \widetilde{f_\theta}[k+1-i] \right)^2, \tag{20}$$

and, hence, each set Φ^p corresponds with the solution of an associated linear least squares problem (20).

To introduce the previously described observed and forecasted values of f_θ within the signal generator description (8), we begin by 'splitting' the time-window Ξ_N as described in Faedo, Peña-Sanchez, and Ringwood (2020), in terms of both estimated $\widetilde{f_\theta}$, and forecasted $\widehat{f_\theta}$ values of the wave excitation torque f_θ. In particular, we define Ξ_N as the following union of sets

$$\Xi_N = \left[N\Delta_h, t_N^m\right] \cup \left(t_N^m, N\Delta_h + T_h\right] = \widetilde{\Xi_N} \cup \widehat{\Xi_N}, \tag{21}$$

where $t_N^m \in \Xi_N$ denotes the current time instant, located at the centre of the window Ξ_N, *i.e.* $t_N^m = T_h/2 + N\Delta_h$, as in Faedo, Peña-Sanchez, and Ringwood (2020). Based on (21), we can associate a corresponding 'total' wave excitation torque estimate for the time-window Ξ_N, *i.e.* $\overline{f_\theta}(t) \in \Xi_N$, by an appropriate combination of $\widetilde{f_\theta}(t) \in \widetilde{\Xi_N}$ and $\widehat{f_\theta}(t) \in \widehat{\Xi_N}$:

$$\overline{f_\theta} = \begin{cases} \widetilde{f_\theta} & \text{if } t \in \widetilde{\Xi_N}, \\ \widehat{f_\theta} & \text{if } t \in \widehat{\Xi_N}. \end{cases} \tag{22}$$

Note that $\widetilde{\Xi_N}$ includes both *past* and *current* estimates of f_θ, while $\widehat{\Xi_N}$ is exclusively characterised in terms of forecasted values of the wave excitation torque. This is illustrated, for the sake of clarity, in Fig. 6 (top), where a specific time-window Ξ_N is presented, showing past, current, and future values of both the target[12] excitation f_θ, and the corresponding estimate $\overline{f_\theta}$ as defined in (22), for one of the sea-states tested experimentally (see Section 5.1 for further detail).

We note that, given the T_h-periodicity associated with the signal generator (8) (see Remark 5), a further step needs to be taken in order to represent the wave excitation estimate (22) in terms of the corresponding solution ξ. In particular, following Faedo, Peña-Sanchez, and Ringwood (2020), we define the so-called apodised wave excitation input:

$$\lfloor \overline{f_\theta} \rfloor = \zeta \overline{f_\theta}, \tag{23}$$

[12] See Section 5.2 for further details on the specific experimental methodology employed to measure the excitation torque for estimator/forecaster validation purposes.

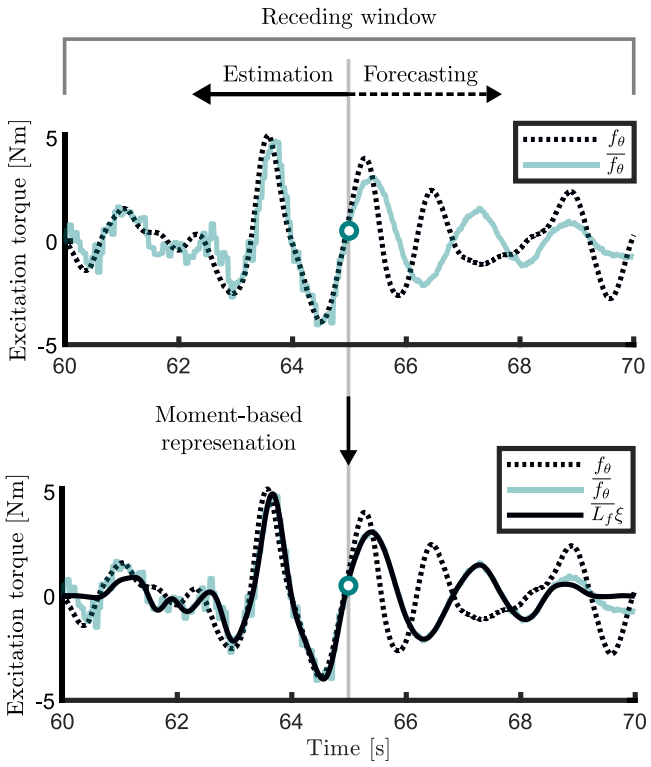

Fig. 6. Wave excitation input representation for each window Ξ_N.

where $\zeta : \Xi_N \to [0, 1]$, $t \mapsto \zeta(t)$, denotes a Planck-taper[13] (McKechan, Robinson, & Sathyaprakash, 2010) apodisation (*i.e.* windowing) map, used to smoothly bring $\overline{f_\theta}$ down to zero at the edges of the set Ξ_N, so that the derivative of its corresponding T_h-periodic extension is sufficiently smooth (Prabhu, 2014). Finally, (23) can be written in terms of ξ in (8), for each time-window Ξ_N, by means of a well-posed least squares procedure: Suppose, for simplicity of exposition, that we consider the same set of collocation points $\mathscr{T}_{\mathscr{C}} \subset \Xi_N$ used to enforce the state and input constraints. Then, the apodised wave excitation estimate $\lfloor \overline{f_\theta} \rfloor$, with $t \in \Xi_N$, can be brought to the form

$$f_\theta \approx \lfloor \overline{f_\theta} \rfloor \mapsto \overline{L_f}\xi, \tag{24}$$

where $\overline{L_f}^{\mathsf{T}} \in \mathbb{R}^\nu$ is given by

$$\begin{aligned} \overline{L_f} &= \Lambda_f \Lambda^{\mathsf{T}} \left(\Lambda\Lambda^{\mathsf{T}}\right)^{-1}, \\ \Lambda_f &= \left[\lfloor \overline{f_\theta} \rfloor(t_1^{\mathscr{C}}) \quad \dots \quad \lfloor \overline{f_\theta} \rfloor(t_{N_{\mathscr{C}}}^{\mathscr{C}}) \right], \end{aligned} \tag{25}$$

with Λ as defined in (14), and where the invertibility of the matrix $\Lambda\Lambda^{\mathsf{T}}$ is guaranteed by the excitability condition on the pair (S, ξ_0) (see Remark 4). A specific example of the resulting representation in (24), arising from the least squares procedure described immediately above, can be seen in Fig. 6 (bottom), where the mapped excitation $\overline{L_f}\xi$ (solid-black line) is shown together with the target wave torque input f_θ (dotted-black line), and the corresponding estimate $\overline{f_\theta}$ (solid-grey line), composed of past, current, and future estimated values of the wave excitation.

Remark 10. The underlying accuracy of the input representation (8)–(24) will depend on both the definition of the time-horizon T_h,

[13] The specific choice of this family of apodisation function is motivated in Faedo, Peña-Sanchez, and Ringwood (2020), and is linked to its capabilities to retain the power spectrum of the signal $\overline{f_\theta}$, being this fundamental to ensure consistency in the energy-maximising control procedure.

Table 2
Sea-states considered for experimental controller testing.

Sea-state	H^w	T^w
SS1	0.052 [m]	1.836 [s]
SS2	0.104 [m]	1.836 [s]
SS3	0.063 [m]	1.412 [s]
SS4	0.104 [m]	1.412 [s]

which is explicitly linked with the fundamental frequency ω_0, and the total number of super-harmonics d, used to define S in (8). Note that the latter has a direct impact on the size of the approximation space spanned by the set $\{\xi_i(t)\}$ (see also Remark 5). These aspects, which are of practical relevance, are discussed in detail within Section 5.4.

Remark 11. With the definition provided in (24)–(25), the incorporation of estimated and forecasted values of the external wave excitation input to the moment-based controller can be performed straightforwardly, by simply replacing L_f with $\overline{L_f}$ for each window Ξ_N, and solve problem $(\overline{P_N})$ in (13) accordingly.

5. Experimental results

This section describes the experimental performance results obtained when considering the energy-maximising moment-based control solution, described in Section 4, for the experimental WEC system (and associated set-up) detailed in Section 2. In particular, the specific set of operating conditions, *i.e.* sea-states, in which the controller is assessed, are detailed in Section 5.1. Since the moment-based controller is synthesised based on the dynamical WEC model identified in Section 3, we dedicate Section 5.2 to provide an assessment, and subsequent validation, for system (4), using representative input/output data collected directly from wave tank experiments. Section 5.3 provides a detailed performance appraisal of both unknown-input estimation (in terms of normalised mean square error) and forecasting strategies (in terms of the well-known 'goodness of fit' indicator), described in Section 4.3, used to provide estimates of f_θ for subsequent controller computation. Finally, Section 5.4 discusses parameter tuning and implementation details for the moment-based controller, while Section 5.5 presents performance assessment and validation of the controller in terms of energy-maximising behaviour, featuring, in addition, a comparison with a well-established benchmark controller.

5.1. Sea-state specifications

The set of sea-states (SS), considered within this paper, is chosen with the main aim of testing and validating the controller performance in a variety of representative operating conditions. To achieve such an objective, four different SS have been selected, based on a JONSWAP (Hasselmann, Barnett, Bouws, Carlson, Cartwright, Eake, Euring, Gicnapp, Hasselmann, Kruseman, et al., 1973) stochastic wave description, with typical peak periods T^w and significant wave heights H^w as detailed in Table 2. The so-called peak enhancement parameter is set to $\gamma^w = 3.3$ for all the considered cases. For each SS, two different realisations of the corresponding stochastic wave process have been considered, each with a total time-length of 350 [s] (which corresponds with more than $\approx$ 200 peak periods for each SS in Table 2), hence guaranteeing statistically consistent performance results for the totality of the considered experimental scenarios.

Fig. 7 shows both theoretical (solid line), and experimental (solid-transparent lines) spectral density functions (SDFs), for each SS (and corresponding set of two realisations). From now on, we use the shorthand notation 'SSXRY' to denote a specific realisation Y of a given sea-state SSX, *e.g.* we use 'SS1R2' to denote realisation number 2 of sea-state 1.

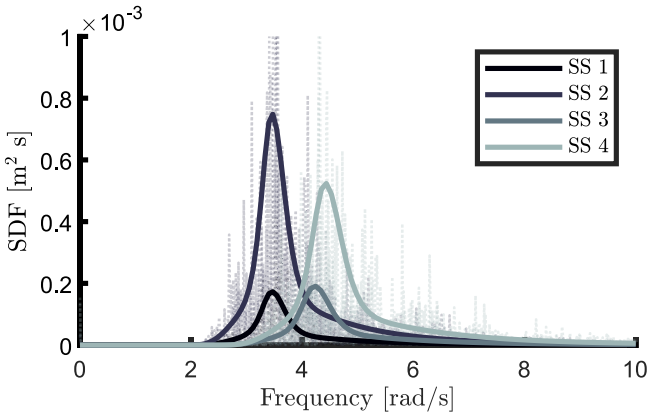

Fig. 7. Theoretical and experimental SDF for each considered SS.

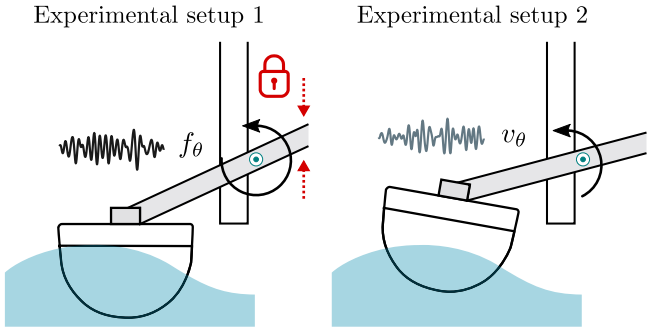

Fig. 8. Experimental setup for wave excitation torque measurement.

Remark 12. The choice of considering two different realisations for each SS is not arbitrary. For instance, given that the wave excitation forecasting strategy requires a set of training data for the computation of the corresponding set of AR coefficients (see Eq. (20)), the use of two different realisations allows us to fully 'decouple' the AR training procedure, by using a completely different realisation for training purposes to that effectively considering when testing the controller, hence always providing practically relevant performance results.

5.2. Model assessment and validation

Assessment and validation of the dynamical structure G_θ in (4), computed following the procedure described in Section 3, necessitates the computation/definition of a set of representative wave excitation inputs f_θ, in order to test the model for each defined operating (SS) conditions. Furthermore, such a set of input signals is also of practical benefit for tuning and validation of both the unknown-input observer, and the AR forecasting strategy, discussed in Section 5.3, providing an appropriate set of 'target' excitation torque signals f_θ for estimator performance assessment, and forecaster training, respectively. Nonetheless, as stressed in Section 4.3, wave excitation force/torque is, in practice, an unmeasurable quantity, since it is effectively impossible to directly 'decouple' the wave excitation force/torque from other (internal) hydrodynamic effects acting on the device while moving under the action of the surrounding wave field (Peña-Sanchez et al., 2019).

To circumvent this issue, and provide a set of measured wave excitation force input signals f_θ, useful both for model, and unknown-input estimator/forecasting validation/training, we lock the physical system mechanically, by locking the device arm accordingly, as schematically illustrated in 'Experimental setup 1' provided in Fig. 8. With the device position locked, we use the load cell sitting on the PTO motor axis

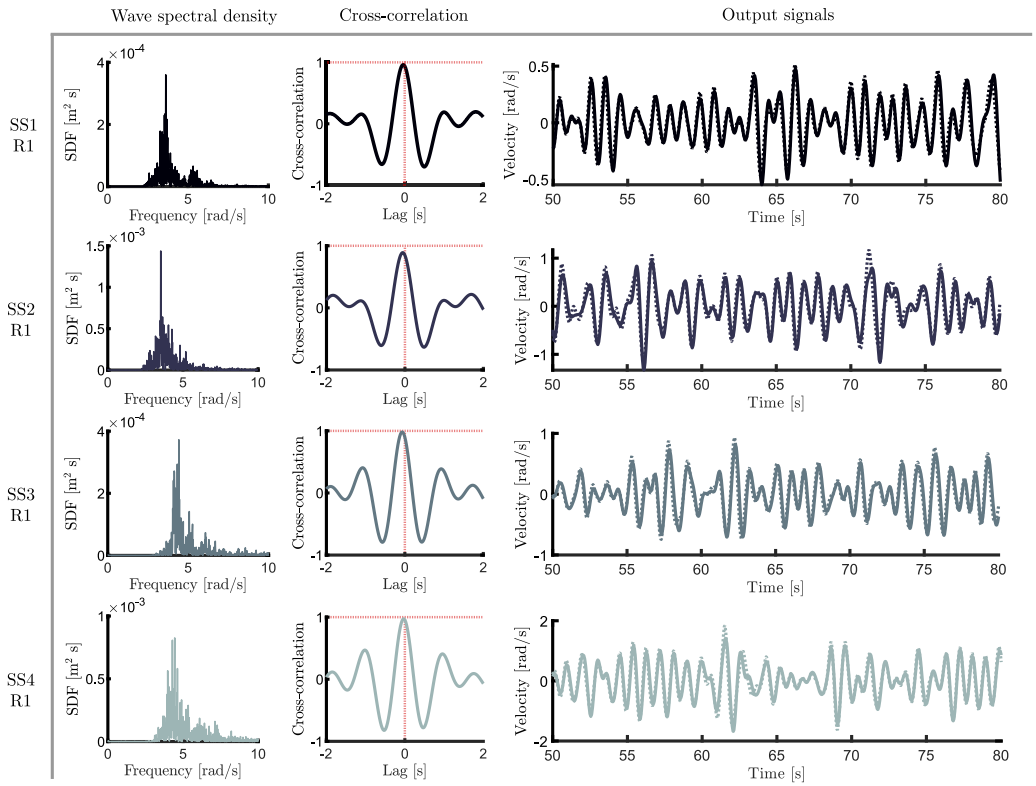

Fig. 9. Time-domain experimental results for model assessment and validation, considering realisation 1 of SS 1 to 4. Within the third column (output signals), dotted lines denote measured experimental velocity, while solid lines are used to represent model response.

(see Section 2) to measure the force time series exerted by each SS and associated realisations, which can be subsequently converted into excitation torque by means of the same algebraic (geometric) map τ considered in Section 3.1 for the system identification procedure (see Remark 2). Relying on the reproducibility capabilities of the wave-tank facilities at Aalborg University, the full set of SS, and their multiple realisations, is repeated with the device free to move, *i.e.* as in 'Experimental setup 2' shown in Fig. 8. Setup 2 is used to measure the associated device motion, *i.e.* the output (angular velocity) v_θ of system (4), corresponding with each SS and realisation considered.

Based on the input/output data collected following the experimental setups described immediately above, Fig. 9 presents time-domain assessment and validation results for the WEC model G_θ, identified as in Section 3. In particular, Fig. 9 shows experimental SDFs associated with SS1R1 to SS1R4 (left), and the resulting cross-correlation functions between measured and model response (middle), and corresponding time-domain measured (dotted lines) and model (solid lines) angular velocities (outputs), for a time window of 30 [s] (right). Note that we omit analysing realisation 2 of each considered SS for economy of space, since the set of results for R2 are similar to those presented for R1, and hence provide an analogous set of assessment metrics.

A first clear conclusion, which can be directly elucidated from the cross-correlation analysis in Fig. 9 (middle), is that the instantaneous phase of both target (measured), and model, output signals, is virtually identical for all the analysed cases, *i.e.* the identified model G_θ in (4) is effectively able to reproduce the phase behaviour of the experimental WEC system accordingly. Note that this feature is of paramount importance within the energy-maximising control design procedure for WECs, given the intrinsic existence of a well-known optimal phase (locking) condition between f_θ and v_θ under optimal control conditions (see Faedo, Carapellese, et al., 2022 and the discussion provided in Section 5.5). Furthermore, as can be appreciated in Fig. 9 (right), the model is effectively able to represent the device motion for the experimental operating conditions considered in this study, retaining both output phase and amplitude fidelity with a satisfactory degree of accuracy.

5.3. Estimator and forecaster validation

Using the target excitation torques, measured as described in Section 5.2, we proceed to present performance results for the unknown-input observer (17), described in Section 4.3. Note that the observer has two main design parameters, *i.e.* the pair of matrices (Q_f, Q_r), which ultimately define the closed-loop behaviour of (17) via the observer gain L_f. To be consistent with realistic WEC operational requirements, where the controller needs to perform well across a variety of sea-states, we use a single fixed pair (Q_f, Q_r) for all the considered experiments. In particular, via iterative calibration over the set of computed signals, we choose $Q_f = 10^{-1}\mathbb{I}_{\tilde{n}}$ and $Q_r = 10^{-5}$, for all the subsequently presented results.

The performance of the estimator is summarised in Fig. 10, in terms of the normalised mean square error (NSME) against experimental data. It can be appreciated that NMSE between target f_θ (measured with the device in blocked position), and estimated signal $\widetilde{f_\theta}$, has a mean of $\approx$ 15% over the totality of analysed experimental sea conditions, denoted with a horizontal green-line in Fig. 10 (left), confirming a satisfactory performance. Furthermore, and for the sake of completeness, Fig. 10 (right) presents a time-snippet of 30 [s] (analogous to Fig. 9) for SS1R1, chosen for its representative NSME, this being the closest to the average value over the total set of experiments.

With respect to the AR forecasting strategy, as described in Section 4.3, the order is fixed to $N_{\text{AR}} = 125$, which effectively coincides with the required number of future samples within each window $\widehat{\Xi_N}$, *i.e.* floor$(T_h/(2\Delta_h))$ (see Section 5.4 for the specification of T_h and Δ_h). The computation of the corresponding set of coefficients, via minimisation of (20), is performed following the arguments posed in Remark 12. In particular, when evaluating the performance of the controller for SSXR1, the AR training procedure is performed using the measured

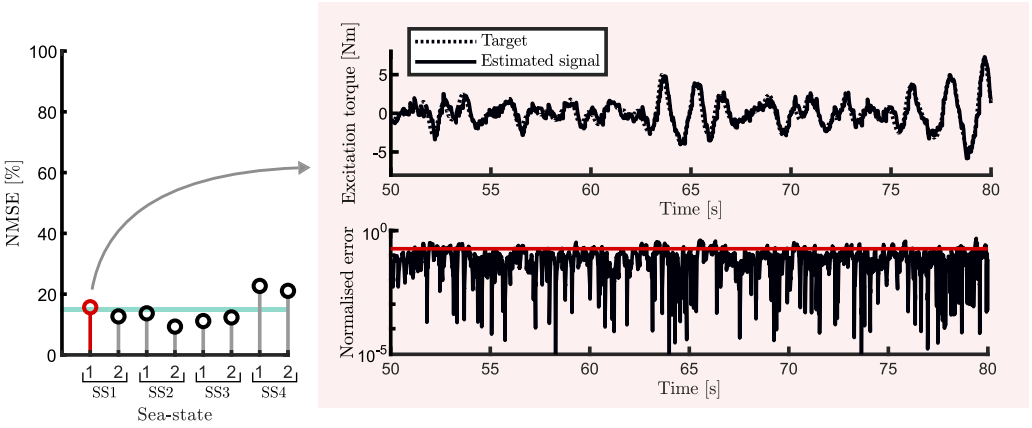

Fig. 10. Performance results for the unknown-input wave excitation torque estimation over the total set of experimental operating conditions.

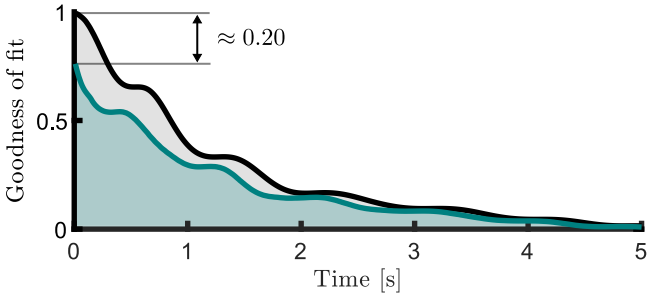

Fig. 11. 'Ideal' (black) and 'real' (green) AR forecasting performance. (For interpretation of the references to colour in this figure legend, the reader is referred to the web version of this article.)

f_θ (as in Section 5.2) for SS*X*R2, and vice-versa. This guarantees a 'decoupling' between AR training, and effective f_θ forecast within the control design procedure. The performance of the forecaster, for SS1, can be appreciated from Fig. 11, in terms of the well-known 'goodness of fit' indicator (as considered in *e.g.* Peña-Sanchez et al. (2018)). In particular, Fig. 11 shows goodness of fit both when predicting the (measured) training data SS1R1, based upon the same set of data, *i.e.* in '*ideal*' (auto-correlation) conditions (black), and when predicting SS1R2 based upon estimated values of the wave excitation torque $\widetilde{f_\theta}$, *i.e.* in '*real*' (cross-correlation) forecast operation conditions (green). Naturally, a loss of performance is to be expected in the latter case, with a drop in goodness-of-fit of about 20% for the 1-step ahead forecast of f_θ. Nonetheless, as discussed in Section 5.5, we show that, even in the presence of such performance degradation, the energy absorption capabilities of the controller are not significantly degraded, consistently outperforming the benchmark case for the full set of experimental scenarios.

5.4. Controller tuning and implementation

As anticipated within Remark 10, the moment-based QP $\overline{(P_N)}$ in (13) has two key tuning parameters: The length of the time-horizon T_h, in which energy is effectively maximised within the corresponding time-window Ξ_N, and the number of super-harmonics d used to defined the corresponding signal generator (8), and hence the corresponding representation of the wave excitation estimate, $\overline{L_f}$, and optimal control input, L_u. We discuss the tuning procedure, adopted within this experimental campaign, in the following paragraphs.

We begin by recalling that T_h directly defines the fundamental frequency $\omega_0 = 2\pi/T_h$, characterising the implicit input description via the signal generator in (8), which, ultimately, defines the approximation space for both the wave excitation force estimate, as computed in the least-square procedure summarised in (24)–(25), and the moment-based optimal control solution u_θ^{opt}. In particular, the larger the value of T_h, the smaller is ω_0, which implies a more refined 'frequency-step' when computing $\{\overline{L_f}, L_u\}$. The selection of T_h, although, is intrinsically connected to the choice of d in (9), *i.e.* the number of harmonics of ω_0 considered to construct the implicit form moment-based representation of the optimal energy-maximising control law. A large value of d increases the quality of the control solution[14] computed via $\overline{(P_N)}$ (see Faedo, Peña-Sanchez, & Ringwood, 2020; Faedo et al., 2018, 2021a), although also having a direct (adverse) impact on the computational complexity of the associated moment-based QP, which is carried out over $\mathbb{R}^\nu$, with $\nu = 2d$.

In practical scenarios, both T_h and d can be tuned together, in terms of a single parameter, which we term the *cut-off* frequency $\omega_c = d\omega_0$, defining the largest multiple of ω_0 used to construct the signal generator (8). In particular, ω_c can be set to a fixed value, corresponding to the largest frequency in which the stochastic description of the set of experimental sea-states present significant energy components. With the value of ω_c effectively fixed, and letting $d = \text{ceil}(T_h\omega_c/2\pi)$, we approach the tuning procedure in simulation (*i.e.* offline), by modifying the time-window length T_h, while monitoring the trade-off between the value of the optimal control objective in $\overline{(P_N)}$ (*i.e.* absorbed energy), and the associated computational requirements.

Within this experimental campaign, and motivated by the stochastic characteristics of the analysed sea-states, we set the cut-off frequency to $\omega_c = 10$ [rad/s], effectively covering the frequency range in which the set of SS present significant (spectral) energy components (see Fig. 7). The time-horizon is set to $T_h = 10$ [s], which corresponds to a fundamental frequency of $\omega_0 \approx 0.63$ [rad/s], and a final number of harmonics $d = 15$. Note that the moment-based QP $\overline{(P_N)}$ in (13) is then carried out over $\mathbb{R}^{30}$.

Remark 13. Given the nature of the least-squares expansion (25), and that of the (harmonic) signal generator (8), the value of the cut-off frequency ω_c can be effectively used with a filtering purpose in mind: Note that the projection (25) emulates a zero-phase (ideal) filtering effect on the wave excitation estimate $\overline{f}_\theta$, within each window Ξ_N. This can be appreciated graphically in Fig. 6 (bottom), where it is clear that any high-frequency (noisy) behaviour in $\overline{f}_\theta$ is effectively 'filtered out' when representing the excitation torque in terms of the solution ξ of (8), making the controller virtually insensitive to noise in $\overline{f}_\theta$, by virtue of a suitable selection of ω_c.

[14] The interested reader is referred to Faedo et al. (2018, Section 5) for an explicit analysis on the relationship between the number of harmonics d, and final energy absorption performance.

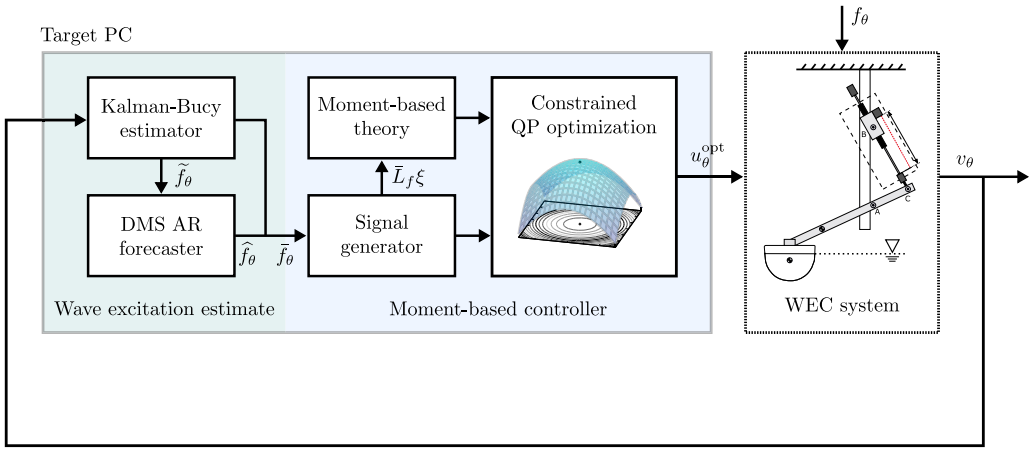

Fig. 12. Schematic illustration of the overall control loop.

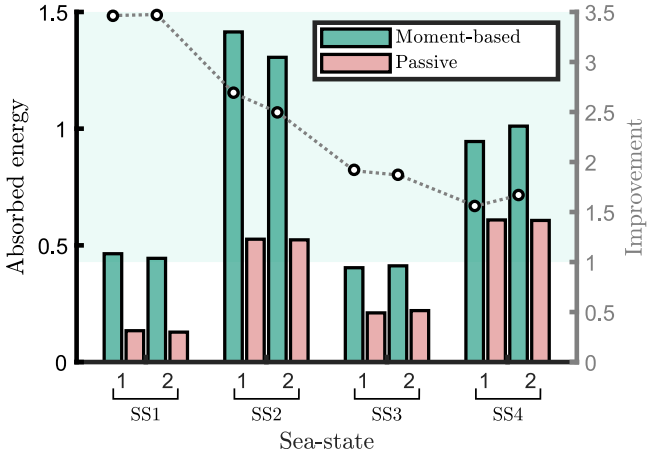

Fig. 13. Experimental performance results for the moment-based control solution, and the benchmark (passive) control case.

The controller sampling time is set to $\Delta_h = 0.04$ [s], which corresponds with a sampling rate of 25 [Hz], consistent with previous literature on experimental testing for the WEC system under scrutiny (see *e.g.* Nguyen et al. (2016)). Note that both the wave excitation torque estimator and AR forecaster are set to have exactly the same sampling rate as the controller, for simplicity of implementation. The uniformly distributed set of time-instants $\mathcal{T}_{\mathscr{C}} \subset \Xi_N$, used to collocate the set of state and input constraints in problem $(\overline{P_N})$, is chosen to have a 'time-step' defined as twice the controller sampling time Δ_h, *i.e.* the cardinality of $\mathcal{T}_{\mathscr{C}}$ is $N_{\mathscr{C}} = T_h/(2\Delta_h) = 125$. The specific values for displacement and control torque limitations, which are defined to respect the physical limitations of the experimental setup described in Section 2 (see also the arguments posed in Ringwood et al. (2017) and Ringwood, Ferri, et al. (2019)), are set to $Z_{\max} = 1$ [rad] and $U_{\max} = 12.5$ [Nm], respectively.

With respect to the specific computation of the numerical solution of problem $(\overline{P_N})$, we implement a primal–dual interior point method (Wright, 1997), adopting a 'warm start' for each Ξ_N. The maximum number of solver iterations is limited to 100, though we clarify that this limit value has never been reached by the controller during the experimental testing phase. Finally, an overall view on the implemented control loop can be appreciated in Fig. 12, including wave excitation estimator and forecaster, and moment-based controller, as structurally implemented in the target PC acting on the WEC system.

5.5. Performance analysis

We summarise, within this section, the performance results obtained by the corresponding moment-based controller,[15] particularly in terms of energy absorption capabilities, which is, effectively, the objective function characterising the WEC OCP (7) (see Section 4.1). Before proceeding with the description of such results, we introduce the well-known 'passive' (proportional) controller, *i.e.*

$$u_\theta = \kappa_{\mathrm{P}}^{\mathrm{SS}\ X} v_\theta, \tag{26}$$

which is adopted as benchmark case for comparison. Note that, aiming to provide a consistent benchmark comparison case, we consider an optimal proportional control structure (26) for each specific sea-state, *i.e.* we design $\kappa_{\mathrm{P}}^{\mathrm{SS}\ X}$ optimally as a function of the specific operating condition, instead of simply fixing a single controller for all the considered sea-states, as is common in the literature. In particular, the set of values $\{\kappa_{\mathrm{P}}^{\mathrm{SS1}}, \kappa_{\mathrm{P}}^{\mathrm{SS2}}, \kappa_{\mathrm{P}}^{\mathrm{SS3}}, \kappa_{\mathrm{P}}^{\mathrm{SS4}}\} \subset \mathbb{R}^+$ is computed via interpolation of the (unconstrained) optimal frequency-domain energy-maximising condition for G_θ, arising from the so-called impedance-matching principle for WEC systems (Faedo, Carapellese, et al., 2022).

Remark 14. Note that, from Table 2, the SS peak frequencies $2\pi/T^w$ can be found at ≈ 3.42 [rad/s], for SS1 and SS2, and close to ≈ 4.45 [rad/s], for the case of SS3 and SS4. In other words, while SS1 and SS2 present significant wave components within the 'low' frequency band, SS3 and SS3 have dominant components closer to the resonance frequency of the WEC system (see the Bode plot in Fig. 4).

From the arguments highlighted in Remark 14, it is expected that the moment-based energy-maximising control solutions for SS1 and SS2 behave more 'aggressively', requiring a larger control effort and reactive power flow to 'enforce resonance' with the incoming wave field, which has significant energy components away from the natural resonant behaviour of the WEC. In contrast, the control solutions for SS3 and SS4 are expected to require significantly less control effort and reactive power flow requirements, since this set of sea-states presents dominant components closer to the resonance frequency of the WEC system, hence automatically requiring less control intervention to achieve energy-maximisation (Faedo, Carapellese, et al., 2022; Faedo, García-Violini, Peña-Sanchez, & Ringwood, 2020). We note that the (unconstrained) energy-maximising solution at resonance can be reasonably realised in terms of a proportional (passive) controller as

[15] The interested reader is referred to Faedo, Pena-Sanchez, and García-Violini (2022) for an illustrative video on the prototype system under moment-based control, as implemented within this experimental campaign.

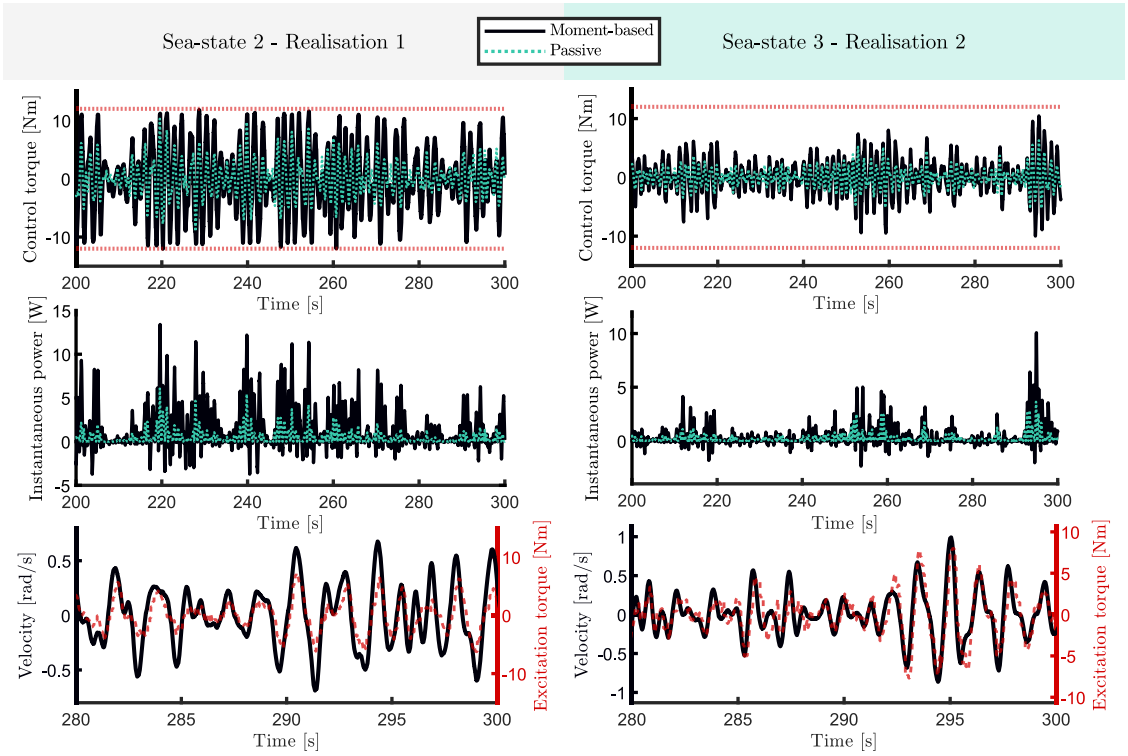

Fig. 14. Time-snippets of control torque (top), instantaneous power (middle), and device velocity under control conditions (bottom), for SS2R1 (left) and SS3R2 (right).

in (26), and it is hence expected that the difference between the benchmark controller (26), and the proposed moment-based approach, is reduced with respect to the performance improvement obtained in SS1 and SS2.

Fig. 13 shows absorbed energy for the complete set of operating conditions, encompassing both moment-based (green), and benchmark (red) passive control results. At a first glance, it is clear that the moment-based optimal controller consistently outperforms the benchmark control strategy, presenting a substantial performance improvement of up to 3.5 times (for SS1) the energy absorbed by the latter. Furthermore, consistently with the discussion and arguments posed in the paragraph immediately above, the increase in performance of the moment-based controller is more pronounced for SS1 and SS2, although always achieving over 1.5 times the energy produced with the passive controller for SS3 and SS4.

Finally, both to emphasise and complement the arguments and results provided up until this point, and illustrate the constraint handling capabilities of the moment-based controller, Fig. 14 shows time-snippets (with a duration of 100 [s]) of control torque (top), instantaneous power (middle), and device velocity under control conditions (bottom), for SS2R1 (left) and SS3R2 (right). Note that, as expected, the moment-based controller (solid-black line) exhibits a significantly larger control effort and reactive power flow requirements for SS2R1, although always operating within the specified torque limit[16] $U_{\max}$ (indicated with a horizontal dotted-red line). In contrast, the moment-based control solution for SS3R2 can be seen to be less 'demanding', presenting a higher degree of similarity with the passive (benchmark) control action (dotted-green line), also consistently with was expected from the arguments exposed previously in this section. As a last performance indicator for the moment-based controller, the well-known energy-maximising 'in-phase' behaviour (see Faedo, Carapellese, et al., 2022) can be appreciated in the motion behaviour of the device under optimal control conditions, where the instantaneous phase of the estimated wave excitation torque is effectively synchronised with that of the WEC velocity, indicating that the controller is actively 'enforcing resonance' with the incoming wave field.

[16] Though displacement constraints have been incorporated within the controller implementation (as detailed in Section 5.4), these have been consistently inactive for all the considered sea-states.

6. Conclusions

Motivated by the demonstrated potential of optimal moment-based control for WEC systems in theory and numerical simulation, we present, in this paper, an experimental assessment and validation of such a control strategy for a prototype Wavestar wave energy converter. In particular, we address the control design and synthesis procedure in an integrated fashion, covering experimental (physically consistent) system identification, unknown-input estimation and forecasting of wave excitation forces, and subsequent control law computation. We demonstrate that the moment-based controller is able to effectively maximise energy-absorption from the wave resource in real-time, with a consistent improvement of up to 3.5 times the energy absorbed by the benchmark controller case, while also being able to handle the user-defined set of constraint specifications throughout the full set of tested operating conditions (SS). The results presented and discussed in this paper demonstrate concrete feasibility of moment-based WEC control, filling the gap between the theoretical aspects associated with such a strategy and the WEC practical application, hence providing a tangible proof of reliability for any potential WEC technology stakeholder. Future work will aim to assess the performance of the robust moment-based solutions for system (Faedo et al., 2019) and input (Faedo, Mattiazzo, & Ringwood, 2022) uncertainty, providing a comparison with the experimental results presented within this study.

Declaration of competing interest

The authors declare that they have no known competing financial interests or personal relationships that could have appeared to influence the work reported in this paper.

Acknowledgements

This project has received funding from the European Union's Horizon 2020 research and innovation programme under the Marie Sklodowska-Curie grant agreements No 101024372 and 101034297. This material has also been supported by Science Foundation Ireland (SFI) through the MaREI Centre for Energy, Climate, and Marine, under grant No. 12/RC/2303_P2.

References

Astolfi, A. (2010). Model reduction by moment matching for linear and nonlinear systems. *IEEE Transactions on Automatic Control*, *55*(10), 2321–2336.

Astolfi, A., Scarciotti, G., Simard, J., Faedo, N., & Ringwood, J. V. (2020). Model reduction by moment matching: Beyond linearity a review of the last 10 years. In *59th IEEE conference on decision and control* (pp. 1–16). IEEE.

Babarit, A., & Delhommeau, G. (2015). Theoretical and numerical aspects of the open source BEM solver NEMOH. In *11th European wave and tidal energy conference, Nantes*.

Bacelli, G., & Ringwood, J. V. (2014). Numerical optimal control of wave energy converters. *IEEE Transactions on Sustainable Energy*, *6*(2), 294–302.

Beatty, S. J., Hall, M., Buckham, B. J., Wild, P., & Bocking, B. (2015). Experimental and numerical comparisons of self-reacting point absorber wave energy converters in regular waves. *Ocean Engineering*, *104*, 370–386.

Cretel, J., Lewis, A., Lightbody, G., & Thomas, G. (2010). An application of model predictive control to a wave energy point absorber. *IFAC Proceedings Volumes*, *43*(1), 267–272.

Davidson, J., Giorgi, S., & Ringwood, J. V. (2015). Linear parametric hydrodynamic models for ocean wave energy converters identified from numerical wave tank experiments. *Ocean Engineering*, *103*, 31–39.

Desoer, C. A., & Vidyasagar, M. (2009). *Feedback systems: input-output properties*. SIAM.

Faedo, N. (2020). *Optimal control and model reduction for wave energy systems: A moment-based approach* (Ph.D. thesis), Department of Electronic Engineering, Maynooth University.

Faedo, N. (2021). LMI-based passivation for LTI systems with application to marine structures - Matlab implementation. http://dx.doi.org/10.5281/zenodo.5797733, Zenodo.

Faedo, N., Carapellese, F., Pasta, E., & Mattiazzo, G. (2022). On the principle of impedance-matching for underactuated wave energy harvesting systems. *Applied Ocean Research*, *118*, Article 102958.

Faedo, N., García-Violini, D., Peña-Sanchez, Y., & Ringwood, J. V. (2020). Optimisation-vs. non-optimisation-based energy-maximising control for wave energy converters: A case study. In *European control conference* (pp. 843–848). IEEE.

Faedo, N., García-Violini, D., Scarciotti, G., Astolfi, A., & Ringwood, J. V. (2019). Robust moment-based energy-maximising optimal control of wave energy converters. In *IEEE 58th conference on decision and control* (pp. 4286–4291). IEEE.

Faedo, N., Giorgi, G., Ringwood, J. V., & Mattiazzo, G. (2022). Optimal control of wave energy systems considering nonlinear Froude-Krylov effects: Control-oriented modelling and moment-based control. *Nonlinear Dynamics*, *109*(3), 1777–1804.

Faedo, N., Mattiazzo, G., & Ringwood, J. V. (2022). Robust energy-maximising control of wave energy systems under input uncertainty. In *2022 European control conference* (pp. 614–619). IEEE.

Faedo, N., Olaya, S., & Ringwood, J. V. (2017). Optimal control, MPC and MPC-like algorithms for wave energy systems: An overview. *IFAC Journal of Systems and Control*, *1*, 37–56.

Faedo, N., Peña-Sanchez, Y., Carapellese, F., Mattiazzo, G., & Ringwood, J. V. (2021). LMI-based passivation of LTI systems with application to marine structures. *IET Renewable Power Generation*, *15*(14), 3424–3433.

Faedo, N., Pena-Sanchez, Y., & García-Violini, D. (2022). Experimental assessment and validation of optimal energy-maximising control: Controlled vs. uncontrolled device motion. http://dx.doi.org/10.5281/zenodo.6595123, Open-access.

Faedo, N., Peña-Sanchez, Y., & Ringwood, J. V. (2020). Receding-horizon energy-maximising optimal control of wave energy systems based on moments. *IEEE Transactions on Sustainable Energy*, *12*(1), 378–386.

Faedo, N., Piuma, F. J. D., Giorgi, G., & Ringwood, J. V. (2020). Nonlinear model reduction for wave energy systems: A moment-matching-based approach. *Nonlinear Dynamics*, *102*(3), 1215–1237.

Faedo, N., & Ringwood, J. V. (2021). A control design framework for wave energy devices. In *4th European wave and tidal energy conference*.

Faedo, N., Scarciotti, G., Astolfi, A., & Ringwood, J. V. (2018). Energy-maximising control of wave energy converters using a moment-domain representation. *Control Engineering Practice*, *81*, 85–96.

Faedo, N., Scarciotti, G., Astolfi, A., & Ringwood, J. V. (2021a). Nonlinear energy-maximizing optimal control of wave energy systems: A moment-based approach. *IEEE Transactions on Control Systems Technology*, *29*(6), 2533–2547.

Faedo, N., Scarciotti, G., Astolfi, A., & Ringwood, J. V. (2021b). On the approximation of moments for nonlinear systems. *IEEE Transactions on Automatic Control*, *66*(11), 5538–5545.

Falnes, J., & Kurniawan, A. (2020). *Ocean waves and oscillating systems: linear interactions including wave-energy extraction, vol. 8*. Cambridge University Press.

García-Violini, D., Faedo, N., & Pena-Sanchez, Y. (2022). Experimental assessment and validation of optimal energy-maximising control: System identification procedure. http://dx.doi.org/10.5281/zenodo.6595150, Open-access.

García-Violini, D., Peña-Sanchez, Y., Faedo, N., Windt, C., Ferri, F., & Ringwood, J. V. (2021). Experimental implementation and validation of a broadband LTI energy-maximizing control strategy for the wavestar device. *IEEE Transactions on Control Systems Technology*, *29*(6), 2609–2621.

García-Violini, D., Pena-Sanchez, Y., Faedo, N., Windt, C., & Ringwood, J. V. (2020). LTI energy-maximising control for the wave star wave energy converter: Identification, design, and implementation. *IFAC-PapersOnLine*, *53*(2), 12313–12318.

Genest, R., & Ringwood, J. V. (2016). Receding horizon pseudospectral control for energy maximization with application to wave energy devices. *IEEE Transactions on Control Systems Technology*, *25*(1), 29–38.

Hansen, R. H., & Kramer, M. M. (2011). Modelling and control of the wavestar prototype. In *Proceedings of the 9th European wave and tidal energy conference*. University of Southampton.

Hasselmann, K. F., Barnett, T. P., Bouws, E., Carlson, H., Cartwright, D. E., Eake, K., et al. (1973). Measurements of wind-wave growth and swell decay during the Joint North Sea Wave Project (JONSWAP). *Ergaenzungsheft Zur Deutschen Hydrographischen Zeitschrift, Reihe A*.

Isidori, A. (2013). *Nonlinear control systems*. Springer Science & Business Media.

Jia, Y., Meng, K., Dong, L., Liu, T., Sun, C., & Dong, Z. Y. (2020). Economic model predictive control of a point absorber wave energy converter. *IEEE Transactions on Sustainable Energy*, *12*(1), 578–586.

Kalman, R. E., & Bucy, R. S. (1961). New results in linear filtering and prediction theory. *Journal of Basic Engineering*, *83*(1), 95–108.

Korde, U. A., & Ringwood, J. V. (2016). *Hydrodynamic control of wave energy devices*. Cambridge University Press.

Li, G. (2017). Nonlinear model predictive control of a wave energy converter based on differential flatness parameterisation. *International Journal of Control*, *90*(1), 68–77.

Li, G., & Belmont, M. R. (2014). Model predictive control of sea wave energy converters–part I: A convex approach for the case of a single device. *Renewable Energy*, *69*, 453–463.

Ling, B. A., Bosma, B., & Brekken, T. K. (2019). Experimental validation of model predictive control applied to the azura wave energy converter. *IEEE Transactions on Sustainable Energy*, *11*(4), 2284–2293.

Ljung, L. (1998). System identification. In *Signal analysis and prediction* (pp. 163–173). Springer.

McKechan, D., Robinson, C., & Sathyaprakash, B. S. (2010). A tapering window for time-domain templates and simulated signals in the detection of gravitational waves from coalescing compact binaries. *Classical and Quantum Gravity*, *27*(8), Article 084020.

Nguyen, H.-N., Sabiron, G., Tona, P., Kramer, M. M., & Vidal Sanchez, E. (2016). Experimental validation of a nonlinear MPC strategy for a wave energy converter prototype. In *International conference on offshore mechanics and arctic engineering, vol. 49972*. American Society of Mechanical Engineers, V006T09A019.

Nguyen, H.-N., & Tona, P. (2017). Wave excitation force estimation for wave energy converters of the point-absorber type. *IEEE Transactions on Control Systems Technology*, *26*(6), 2173–2181.

Padoan, A., Scarciotti, G., & Astolfi, A. (2017). A geometric characterization of the persistence of excitation condition for the solutions of autonomous systems. *IEEE Transactions on Automatic Control*, *62*(11), 5666–5677.

Peña-Sanchez, Y., Mérigaud, A., & Ringwood, J. V. (2018). Short-term forecasting of sea surface elevation for wave energy applications: The autoregressive model revisited. *IEEE Journal of Oceanic Engineering*, *45*(2), 462–471.

Pena-Sanchez, Y., García-Violini, D., & Faedo, N. (2022). Experimental assessment and validation of optimal energy-maximising control: Overview of wave tank facilities. http://dx.doi.org/10.5281/zenodo.6595097, Open-access.

Peña-Sanchez, Y., Windt, C., Davidson, J., & Ringwood, J. V. (2019). A critical comparison of excitation force estimators for wave-energy devices. *IEEE Transactions on Control Systems Technology*, *28*(6), 2263–2275.

Prabhu, K. M. (2014). *Window functions and their applications in signal processing*. Taylor & Francis.

Richter, M., Magana, M. E., Sawodny, O., & Brekken, T. K. (2012). Nonlinear model predictive control of a point absorber wave energy converter. *IEEE Transactions on Sustainable Energy*, *4*(1), 118–126.

Ringwood, J. V. (2020). Wave energy control: Status and perspectives 2020. *IFAC-PapersOnLine*, *53*(2), 12271–12282.

Ringwood, J., Bacelli, G., & Fusco, F. (2014). Energy-maximizing control of wave-energy converters: The development of control system technology to optimize their operation. *IEEE Control Systems*, *34*(5), 30–55.

Ringwood, J., Ferri, F., Ruehl, K. M., Yu, Y.-H., Coe, R. G., Bacelli, G., et al. (2017). A competition for WEC control systems. In *Proceedings of the 12th European wave and tidal energy conference 27th Aug-1st Sept 2017, no. 831* (pp. 1–9). European Wave and Tidal Energy Conference 2017.

Ringwood, J., Ferri, F., Tom, N., Ruehl, K., Faedo, N., Bacelli, G., et al. (2019). The wave energy converter control competition: Overview. In *International conference on offshore mechanics and arctic engineering, vol. 58899*. American Society of Mechanical Engineers, V010T09A035.

Ringwood, J. V., Mérigaud, A., Faedo, N., & Fusco, F. (2019). An analytical and numerical sensitivity and robustness analysis of wave energy control systems. *IEEE Transactions on Control Systems Technology*, *28*(4), 1337–1348.

Scruggs, J., Lattanzio, S., Taflanidis, A., & Cassidy, I. (2013). Optimal causal control of a wave energy converter in a random sea. *Applied Ocean Research*, *42*, 1–15.

Tom, N., & Yeung, R. W. (2015). Experimental confirmation of nonlinear-model-predictive control applied offline to a permanent magnet linear generator for ocean-wave energy conversion. *IEEE Journal of Oceanic Engineering*, *41*(2), 281–295.

Tona, P., Sabiron, G., Nguyen, H.-N., Mérigaud, A., & Ngo, C. (2020). Experimental assessment of the IFPEN solution to the WEC control competition. In *International conference on offshore mechanics and arctic engineering, vol. 84416*. American Society of Mechanical Engineers, V009T09A023.

Umeda, J., Goto, H., Fujiwara, T., Taniguchi, T., & Inoue, S. (2018). Experimental study on model predictive control for a point absorber type wave energy converter with a linear generator. In *International conference on offshore mechanics and arctic engineering, vol. 51319*. American Society of Mechanical Engineers, V010T09A027.

Van Overschee, P., & De Moor, B. (2012). *Subspace identification for linear systems: theory—implementation—applications*. Springer Science & Business Media.

Vavasis, S. A. (2001). Complexity theory: Quadratic programming. In C. A. Floudas, & P. M. Pardalos (Eds.), *Encyclopedia of optimization* (pp. 304–307). Springer US.

WavEnergy Wiki. (2022). https://wavenergy.wiki/september-2021-the-experimental-campaign/. (Accessed 08 September 2022).

WavEnergy YouTube Channel. (2022). https://www.youtube.com/channel/UCNB74IeIeZFobaQxSHy5u8g. (Accessed 08 September 2022).

Windt, C., Faedo, N., Penalba, M., Dias, F., & Ringwood, J. V. (2021). Reactive control of wave energy devices–The modelling paradox. *Applied Ocean Research*, *109*, Article 102574.

Wright, S. J. (1997). *Primal-dual interior-point methods*. SIAM.

Zhan, S., Li, G., & Bailey, C. (2019). Economic feedback model predictive control of wave energy converters. *IEEE Transactions on Industrial Electronics*, *67*(5), 3932–3943.